CrossMark

Numerical simulations of three-dimensional foam by the immersed boundary method

Yongsam Kim [a],[*], Ming-Chih Lai [b], Charles S. Peskin [c], Yunchang Seol [a]

[a] *Department of Mathematics, Chung-Ang University, Dongjakgu Heukseokdong, Seoul 156-756, Republic of Korea*
[b] *Department of Applied Mathematics, Institute of Mathematical Modeling and Scientific Computing, National Chiao Tung University, 1001, Ta Hsueh Road, Hsinchu 300, Taiwan*
[c] *Courant Institute of Mathematical Sciences, New York University, 251 Mercer Street, New York, NY 10012, USA*

A R T I C L E   I N F O

A B S T R A C T

In this paper, we extend (Kim et al., 2010 [13]) to the three-dimensional dry foam case, i.e., a foam in which most of the volume is attributed to its gas phase. Dry foam dynamics involves the interaction between a gas and a collection of thin liquid–film internal boundaries that partitions the gas into discrete cells or bubbles. The liquid–film boundaries are flexible, contract under the influence of surface tension, and are permeable to the gas which moves across them by diffusion at a rate proportional to the local pressure difference across the boundary. Such problems are conventionally studied by assuming that the pressure is uniform within each bubble. Here, we introduce instead an immersed boundary method that takes into account the non-equilibrium fluid mechanics of the gas. To model gas diffusion across the internal liquid–film boundaries, we allow normal slip between the boundary and the gas at a velocity proportional to the (normal) force generated by the boundary surface tension. We implement this method in the three-dimensional framework, and test it by verifying the 3D generalization of the von Neumann relation, which governs the coarsening of a three-dimensional dry foam.

© 2014 Elsevier Inc. All rights reserved.

1. Introduction

We use an immersed boundary (IB) method to simulate a "dry" foam in 3D, i.e., a gas–liquid mixture in which most of the volume is attributed to its gas phase. One interesting phenomenon, which is called diffusive coarsening, is the evolution in bubble size and topological structure that occurs as a result of gas exchange between bubbles [1]. This gas exchange occurs by diffusion through the thin liquid films that separate one bubble from another. The diffusive flux of gas through such a film is proportional to the pressure difference between the two bubbles that are separated by that film. In a dry foam, those thin films forming the faces of the roughly polyhedral bubbles are called "lamella", and the junctions of these films are called "Plateau borders" which form the tubes in which liquid may flow. The vertices, at which typically four Plateau borders intersect, are called "nodes".

In 1952, von Neumann [2,3] showed that the rate of change of the area of a given bubble (a curved polygon) in a two-dimensional dry foam is independent of bubble size and solely dependent on the number of walls (or edges). The derivation of this remarkable result is based on the fact that the net rate of outward diffusion of gas per unit length
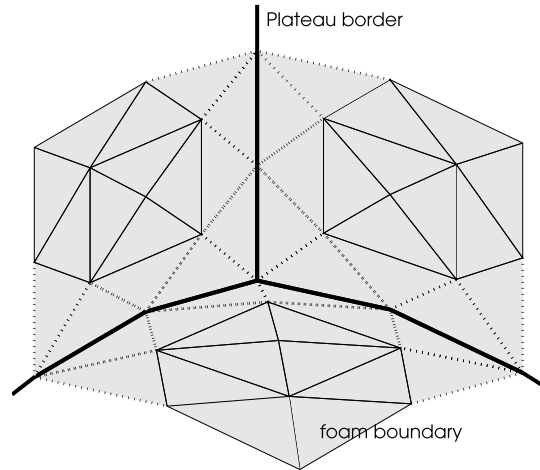
Fig. 1. Schematic figure of foam boundaries composed of three surfaces. The surfaces, which are modeled as triangular facets, meet at Plateau borders (bold lines). An edge of a triangle can be a part of the Plateau borders (bold lines, E_2), have only one vertex on a Plateau border (dotted lines, E_1), and have both vertices in the interior of some face (solid lines, E_0).

through a wall of the (two-dimensional) bubble is proportional to the pressure difference across that wall, which in turn is equal to the product of the surface tension γ and the curvature κ. The rate of change of the area of a bubble is

$$\frac{dA}{dt} = M\gamma \int_{\Gamma} \kappa \, dl = 2\pi M\gamma (n/6 - 1),$$ (1)

where M is a permeability coefficient, the curve Γ is the closed boundary of the bubble, dl is the arc length along Γ, and n is the number of walls. The second equality can be proved by using the fact that the boundary of the bubble is a closed curve and that each of the exterior (turning) angles at the vertex (triple junction) must be equal to $2\pi/6$. Thus, the two-dimensional von Neumann law is purely topological, since the rate of change of area of any particular bubble depends only on its number of edges (the constants M and γ being the same for all of the bubbles in a given foam).

In 3D, the net rate of outward diffusion of gas per unit area through a wall of the bubble is proportional to γH where H is the so-called mean curvature, that is the sum of the two principal curvatures of the wall surface. Let $S(t)$ be the surface of a bubble, and let $V(t)$ be the enclosed volume, then the rate of change of volume of the bubble is

$$\frac{dV}{dt} = M\gamma \iint_{S(t)} H \, dS,$$ (2)

where dS is the area element on $S(t)$. The sign convention for H is that inward curvature is considered to be negative. Note that the integral in (2) is to be understood as the sum of the corresponding integrals over each of the smooth faces of the bubble; there is no contribution from the Plateau borders or from the nodes, where the curvature is infinite, but where gas transport is considered negligible.

It has been a long-standing mathematical problem to establish an explicit formula for the surface integral of the mean curvature along a given surface $S(t)$. Based on the assumption that each of the dihedral angles along junction edge is equal to $2\pi/6$ and on the ingeniously defined mean width of a bubble domain, MacPherson and Srolovitz [4] have derived a general formula for the 3D von Neumann relation, see [4] and its supplementary material.

In the present paper, we derive a discretized version of the 3D von Neumann relation. Let the foam boundary $S(t)$ be modeled as a faceted surface, with triangular facets. Then the discretized version of the 3D von Neumann relation can be written as

$$\frac{dV}{dt} = -M\gamma \sum_{e \in E_0} L_e \theta_e - \frac{M\gamma}{2} \sum_{e \in E_1} L_e \theta_e,$$ (3)

where L_e is the length of edge e of the faceted surface, and θ_e is the angle between the two facets with the same edge e. Here, $\theta_e > 0$ if edge e is convex when viewed from outside the surface. The set E_i, where $i = 0$, 1, or 2, is the collection of edges which have exactly i of their two vertices on a junction edge, which is defined as an edge on which three or more facets meet, see Fig. 1. Thus a junction edge is part of a Plateau border (see above). Such an edge belongs to three or more faces of the foam. It is member of the set E_2 (bold lines), and, as such, it does not appear at all on the right-hand side of (3). An edge in E_1 (dotted lines) share only one vertex with a Plateau border, and an edge in E_0 (solid lines) has both

vertices in the interior of some face. The detailed derivation of the formula (3) is given in Appendix B, and it is used for comparison with our computational results. A similar formula can also be found in [5].

In [1,6–8], the authors simulated the evolution of a two-dimensional dry foam within the framework of the following assumptions: Laplace–Young condition, Plateau's rule, and the von Neumann relation (1). There are other foam simulations that take the fluid dynamics into account. In [9], a numerical study based on a boundary integral formulation is presented to simulate two-dimensional, doubly periodic, diluted and concentrated emulsions or foams structures in a simple shear Stokes flow. Recent work in [10] used a nonsingular boundary integral method to simulate the three-dimensional wet foam drop formation and its dynamics in simple shear flow. More numerical works on the two- and three-dimensional dry or wet foams can also be found in [11,12] and the reference therein.

In [13], three of the present authors have introduced an immersed boundary (IB) method to simulate the fluid dynamics of a two-dimensional dry foam by modeling the gas phase of the foam as a viscous incompressible fluid, and the liquid phase as a massless network of permeable internal boundaries under surface tension. The gas diffusion through the liquid phase of the foam was modeled by allowing the internal boundaries to slip relative to the fluid, at a velocity (speed *and* direction) proportional to the boundary force [13–15]. The paper [13] has shown that the IB method is a proper tool to simulate the 2D foam dynamics by verifying the 2D von-Neumann relation (1) and simulating foams with an arbitrary shape.

Here we extend the methodology introduced in [13] and present the IB method to study the three-dimensional dry foam dynamics. Although we basically use the same idea as in [13], the mathematical derivation and numerical implementation are complicated enough to require a separate detailed description. In 3D, the bubble boundaries are surfaces which we model by triangulation, and the discrete force density has to be evaluated at the vertices of the triangles. The derivation of this discrete force density from the surface energy defined on the triangulated surface is given in Appendix A. Moreover, an algorithm is needed to maintain the resolution of each internal boundary within predetermined bounds despite large changes in the lengths of edges and in the areas of the triangular facets.

The rest of the paper is organized as follows. In Section 2, we describe the equations of motion of the foam in immersed boundary formulation. These are the typical IB equations of motion, generalized to handle a permeable boundary under surface tension. The numerical implementation including external boundary conditions is described in Section 3. In Section 4, we validate the method by doing a convergence study and by showing numerically that the discretized 3D von Neumann relation (3) is satisfied. Then we consider two more complicated cases: one is the case in which a dynamic non-equilibrium flow of gas interacts with the foam boundaries, and the other case involves a foam with multiple bubbles. Conclusions and future work are discussed in Section 5.

2. Equations of motion

In this section, we state the equations of motion of a three-dimensional dry foam, in which the boundaries between bubbles are idealized as massless surfaces under a constant surface tension γ. These boundaries are assumed permeable to the gas phase of the foam, with permeability coefficient M. The gas phase is modeled as a viscous incompressible fluid [13]. The constant density and viscosity of the gas are denoted by ρ and μ, respectively.

In the following formulation, the parameter pair (r, s) labels a material point of an internal foam boundary. We assume that distinct points of the parameter pair (r, s) are used for the different internal foam boundaries, so that any particular value of (r, s) occurs on at most one internal boundary. An integral with respect to (r, s) with no specific limit of integration should be understood as an integral over the union of all of the internal foam boundaries. Thus, we write the equations of motion as follows.

$$\rho \left(\frac{\partial \mathbf{u}}{\partial t} + \mathbf{u} \cdot \nabla \mathbf{u} \right) = -\nabla p + \mu \nabla^2 \mathbf{u} + \mathbf{f}, \tag{4}$$

$$\nabla \cdot \mathbf{u} = 0, \tag{5}$$

$$\mathbf{F}(r, s, t) = -\frac{\partial E}{\partial \mathbf{X}}, \tag{6}$$

$$\mathbf{f}(\mathbf{x}, t) = \int \mathbf{F}(r, s, t) \delta(\mathbf{x} - \mathbf{X}(r, s, t)) \, dr \, ds, \tag{7}$$

$$\frac{\partial \mathbf{X}}{\partial t}(r, s, t) = \mathbf{U}(r, s, t) + M\mathbf{F} \Big/ \left| \frac{\partial \mathbf{X}}{\partial r} \times \frac{\partial \mathbf{X}}{\partial s} \right|,$$

$$= \int \mathbf{u}(\mathbf{x}, t) \delta(\mathbf{x} - \mathbf{X}(r, s, t)) \, d\mathbf{x} + M\mathbf{F} \Big/ \left| \frac{\partial \mathbf{X}}{\partial r} \times \frac{\partial \mathbf{X}}{\partial s} \right|, \tag{8}$$

Eqs. (4)–(5) are the familiar Navier–Stokes equations for a viscous incompressible fluid. The unknown functions in the fluid equations are the fluid velocity, $\mathbf{u}(\mathbf{x}, t)$; the fluid pressure, $p(\mathbf{x}, t)$; and the force density applied by the immersed boundary to the fluid, $\mathbf{f}(\mathbf{x}, t)$, where $\mathbf{x} = (x, y, z)$ are Cartesian coordinates, and t is the time.

Eq. (6) defines the force density which is transmitted by the foam boundary $\mathbf{X}(r, s, t)$ to the fluid, in the sense that $\mathbf{F}(r, s, t)\, dr\, ds$ is the force applied to the fluid by the patch of immersed boundary $dr\, ds$. From Eq. (6), the force density $\mathbf{F}$ is given by $-\frac{\partial E}{\partial \mathbf{X}}$, where $\frac{\partial E}{\partial \mathbf{X}}$ denotes the variational derivative of the elastic energy functional

$$E\big[\mathbf{X}(\cdot, \cdot, t)\big] = \gamma \int \left| \frac{\partial \mathbf{X}}{\partial r} \times \frac{\partial \mathbf{X}}{\partial s} \right| dr\, ds, \tag{9}$$

which is simply the constant surface tension γ times the total surface area of the internal foam boundaries. It can be shown (see Appendix A) that the force applied by the patch $dr\, ds$ to the surrounding fluid is given by

$$\mathbf{F}\, dr\, ds = \gamma H \left(\left| \frac{\partial \mathbf{X}}{\partial r} \times \frac{\partial \mathbf{X}}{\partial s} \right| dr\, ds \right) \mathbf{n}, \tag{10}$$

where $\mathbf{n}$ is the normal vector pointing toward the outside of the surface. It is important to note that, from (10), the boundary force density $\mathbf{F}$ is normal to the boundary, which makes it possible to simplify the formulation of the problem, as explained in more detail below. For the numerical implementation discussed in Section 3, however, we do not compute the force density from the mean curvature directly. Since the foam boundary is described by a triangulation, the discrete version of force density can be derived from the gradient of the corresponding discrete energy functional, see Appendix A as well. In this way we avoid explicit evaluation of the mean curvature in our numerical scheme.

Eqs. (7) and (8) both involve the three-dimensional Dirac delta function $\delta(\mathbf{x}) = \delta(x)\delta(y)\delta(z)$, which express the local character of the interaction between the fluid and boundary. Eq. (7) simply expresses the relation between the two corresponding force densities $\mathbf{f}(\mathbf{x}, t)\, d\mathbf{x}$ and $\mathbf{F}(r, s, t)\, dr\, ds$. Since the function $\delta(\mathbf{x})$ is the three-dimensional Dirac delta function (which has units of reciprocal volume), and since the integral $dr\, ds$ in Eq. (7) is only two-dimensional, the force per unit volume $\mathbf{f}(\mathbf{x}, t)$ is singular like a one-dimensional delta function, and has the character of a delta-function layer with support on the surfaces of the bubbles of the foam. The Lagrangian force density $\mathbf{F}(r, s, t)$, by contrast, is non-singular.

Eq. (8) is the equation of motion of the immersed foam boundary in which M is the permeability constant. To derive Eq. (8), we assume that the gas (fluid) goes through the liquid–film boundary only in the normal direction. Now consider a patch of the boundary of which the area is $\left| \frac{\partial \mathbf{X}}{\partial r} \times \frac{\partial \mathbf{X}}{\partial s} \right| dr\, ds$. The net amount of gas per unit time transported through the patch will be proportional to the pressure difference and the area of the patch. This means that the flux through the patch is equal to

$$M(p_1 - p_2) \left| \frac{\partial \mathbf{X}}{\partial r} \times \frac{\partial \mathbf{X}}{\partial s} \right| dr\, ds, \tag{11}$$

where M is the permeability, and p_1 and p_2 are the pressures on the two sides of the foam boundary, respectively. We assume here that the thickness of the foam boundary is constant. (Otherwise, the flux could also be inversely proportional to the thickness of the foam boundary, and the permeability M could vary depending on the thickness.)

The flux through the patch can also be evaluated by considering the difference between the fluid velocity $\mathbf{U}(r, s, t)$ at the internal boundary and the velocity $\frac{\partial \mathbf{X}}{\partial t}(r, s, t)$ of the boundary itself. That is, the flux can be written as

$$\mathbf{n}(r, s, t) \cdot \left(\mathbf{U}(r, s, t) - \frac{\partial \mathbf{X}}{\partial t}(r, s, t) \right) \left| \frac{\partial \mathbf{X}}{\partial r} \times \frac{\partial \mathbf{X}}{\partial s} \right| dr\, ds, \tag{12}$$

where $\mathbf{n}(r, s, t)$ is the unit normal to the internal boundary. Setting the above two expressions (11) and (12) for the flux equal to each other, we get

$$M(p_1 - p_2) = \mathbf{n}(r, s, t) \cdot \left(\mathbf{U}(r, s, t) - \frac{\partial \mathbf{X}}{\partial t}(r, s, t) \right). \tag{13}$$

From the normal component of mechanical equilibrium at the foam boundary, we see that the pressure jump $(p_1 - p_2)$ can be related to the normal component of the boundary force $\mathbf{F}(r, s, t)$ [16,17] as

$$(p_1 - p_2) \left| \frac{\partial \mathbf{X}}{\partial r} \times \frac{\partial \mathbf{X}}{\partial s} \right| + \mathbf{F}(r, s, t) \cdot \mathbf{n} = 0. \tag{14}$$

Combining these equations and using the fact that $\mathbf{F}(r, s, t)$ is normal to the boundary as discussed above, we obtain Eq. (8)

$$\left(\frac{\partial \mathbf{X}}{\partial t}(r, s, t) - \mathbf{U}(r, s, t) \right) = M\mathbf{F}(r, s, t) \Big/ \left| \frac{\partial \mathbf{X}}{\partial r} \times \frac{\partial \mathbf{X}}{\partial s} \right|. \tag{15}$$

Note that the *tangential* no-slip condition is automatically satisfied in Eq. (15), i.e.,

$$\left(\frac{\partial \mathbf{X}(r, s, t)}{\partial t} - \mathbf{U}(r, s, t) \right) \cdot \boldsymbol{\tau} = 0. \tag{16}$$

One can see that our IB formulation has the advantage of no need to evaluate the pressure differences between bubbles in order to move the internal boundaries of the foam, since the relative slip between such a boundary and the fluid can be found directly from the boundary force. This is important, since the pressure is only computed on the uniform grid that is used for the fluid mechanics (see next section), and the internal boundaries of the foam cut through this grid without being constrained to conform to it in any way, so the direct evaluation of the fluid pressure on the two sides of an internal boundary would require some sort of extrapolation procedure. This is completely avoided here, since our formulation makes no explicit reference to the pressure at all.

3. Numerical scheme

3.1. Computational procedure

What has been stated so far is the mathematical formulation of the problem in immersed boundary form (i.e., with delta-function forces instead of explicit boundary conditions). For the numerical implementation, we use a first-order IB method, generalized to take a permeable foam boundary into account [13,14]. We use a superscript to denote the time level; thus, $\mathbf{X}^n(r, s)$ is a shorthand for $\mathbf{X}(r, s, n\Delta t)$, where Δt is the duration of the time step, and similarly for all other variables.

Throughout this section, we simplify the notation by considering only one of the internal boundaries of the foam. Since there are many such internal boundaries, the numerical procedures we describe below, in particular Steps 1, 2, and 4, need to be applied to all of them. Each internal boundary of the foam is to be represented by a triangulated surface. Let an index k be assigned to each node of this triangulated surface, so that $\mathbf{X}_k^n$ denotes the position of node k at time level n. Let an index f be assigned to each triangulated facet, and let facets(k) denote the set of all facets that touch node k. For $f \in \text{facets}(k)$, let $(\mathbf{X}_k^n, \mathbf{X}_{f,k,2}^n, \mathbf{X}_{f,k,3}^n)$ be the locations at time level n of the three vertices of facet f.

The step-by-step procedure for the time integration from time level n to time level $n+1$ can be summarized as follows.

Step 1. Using the position of the internal boundary $\mathbf{X}^n$, we calculate the Lagrangian force density $\mathbf{F}^n$. This is done as follows:

$$\mathbf{F}_k^n(\Delta A)_k = \sum_{f \in \text{facets}(k)} \frac{\gamma}{2} \big(\mathbf{X}_{f,k,3}^n - \mathbf{X}_{f,k,2}^n\big) \times \mathbf{n}_f^n, \tag{17}$$

where $\mathbf{n}_f^n = (\mathbf{X}_{f,k,2}^n - \mathbf{X}_k^n) \times (\mathbf{X}_{f,k,3}^n - \mathbf{X}_k^n)/|(\mathbf{X}_{f,k,2}^n - \mathbf{X}_k^n) \times (\mathbf{X}_{f,k,3}^n - \mathbf{X}_k^n)|$ is the unit normal to the triangle f, see Appendix A. Note that the order of the vertices in a facet does not matter. If we interchange the subscripts 2 and 3 in the above equations, $(\mathbf{X}_{f,k,3}^n - \mathbf{X}_{f,k,2}^n)$ and $\mathbf{n}_f^n$ both change sign, so each term in Eq. (17) remains the same as before. Conceptually $(\Delta A)_k$ is the amount of Lagrangian area $dr\,ds$ associated with node k. No precise definition is needed for $(\Delta A)_k$, however, since the quantity that we actually use is not the Lagrangian force density $\mathbf{F}_k$, but instead the Lagrangian *force* $\mathbf{F}_k(\Delta A)_k$, and this force is unambiguously defined by Eq. (17), even though the individual factors $\mathbf{F}_k$ and $(\Delta A)_k$ are not.

Step 2. Distribute this force $\mathbf{F}_k^n(\Delta A)_k$ defined on Lagrangian grid points into the force density at Eulerian spatial grid points to be applied in the Navier–Stokes equations. This is done by a discretization of Eq. (7) as

$$\mathbf{f}^n(\mathbf{x}) = \sum_k \mathbf{F}_k^n(\Delta A)_k \delta_h\big(\mathbf{x} - \mathbf{X}_k^n\big), \tag{18}$$

where $\mathbf{x} = (x_1, x_2, x_3)$ is the fluid mesh point, and δ_h is the smooth version of Dirac delta function [18,19].

Step 3. Given the Eulerian force density $\mathbf{f}^n(\mathbf{x})$, we are ready to solve the discretized version of the fluid equations (4)–(5). In the present work, we employ a finite difference solver for the incompressible Navier–Stokes equations which is designed to improve the volume conservation [13,16]. With the periodic boundary conditions, the discretized fluid equations which become linear systems are solved using discrete Fourier transform methodology.

Step 4. Move the foam boundary points by the updated local fluid velocity with a relative slip correction. This is done by approximating Eq. (8) as follows:

$$\frac{\mathbf{X}_k^{n+1} - \mathbf{X}_k^n}{\Delta t} = \sum_{\mathbf{x}} \mathbf{u}^{n+1}(\mathbf{x}) \delta_h\big(\mathbf{x} - \mathbf{X}_k^n\big) h^3 + M \frac{\mathbf{F}_k^n(\Delta A)_k}{\sum_{f \in \text{facets}(k)} \frac{1}{3}|T_f^n|}. \tag{19}$$

Here the notation $|T_f^n|$ denotes the area of facet f at time level n. Note that the value $\sum_{f \in \text{facets}(k)} \frac{1}{3}|T_f^n|$, which is one-third of the total area of the triangular facets f that touch vertex k (a facet has three different vertices), is the discrete approximation to the area element $|\frac{\partial \mathbf{X}}{\partial r} \times \frac{\partial \mathbf{X}}{\partial s}|\,dr\,ds$ at $\mathbf{X}_k^n$ in Eq. (8).
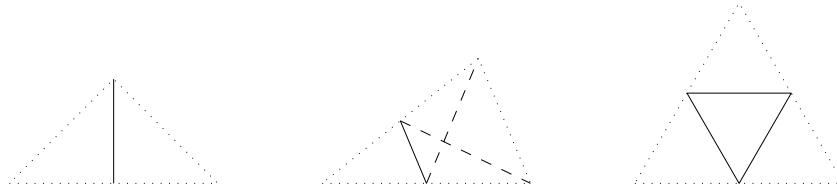
Fig. 2. Refinement of edges and triangles. A new immersed boundary point may be created at the midpoint of any edge of a triangle. When one new vertex is created (left panel), the new vertex is connected (solid line) to the opposite vertex of the original triangle, thus forming two new triangles. When two new vertices are created (middle panel), they are connected (solid line), which divides the original triangle into a triangle and a quadrilateral, and then the quadrilateral is partitioned into two triangles by the shorter one of its two diagonals (dashed lines). When three new vertices are created (right panel), all possible pairs of new vertices are connected (solid lines), and this divides the original triangle into four triangles.

3.2. Some implementation details

3.2.1. No permeability at the junction edges (Plateau borders) or at the nodes, where the junction edges meet

We assume that there is no permeability along the junction edges at which three (or possibly more) internal boundary surfaces meet. Similarly, we assume no permeability at the nodes where the junction edges meet. These junctions and nodes simply move at the local fluid velocity, that is, by Eq. (19) with $M = 0$. To allow permeability along the junction edges or at the nodes would result in inconsistencies, since the normal direction is not uniquely defined there. Physically, the lack of permeability at junction edges and nodes is enforced by an accumulation of liquid, resulting in a slight thickening and smoothing of junction edges and nodes.

3.2.2. The maintenance of foam internal boundary resolution

Since the internal boundary points $\mathbf{X}_k$ of the foam move without any constraint on the length of the edges of each triangle, we need to address the important issue how to maintain reasonable resolution over the surface of the internal boundary. If the resolution becomes too coarse, there will be leaks through the boundary surfaces, and if it becomes too fine, there will be too severe a constraint on the time step to maintain numerical stability. We maintain proper resolution of the boundary surface by simply adding or deleting immersed boundary points (and thus the triangles) as needed, in the following way.

At each time step, we scan the triangles representing internal boundary surface to check the lengths of the edges of each triangle. Let the end points of an edge of a triangle be $\mathbf{X}_1$ and $\mathbf{X}_2$. Whenever $|\mathbf{X}_1 - \mathbf{X}_2| > h/2$, we create a new immersed boundary point halfway between them. Because one triangle has three edges, one, two, or three edges can satisfy the condition for the creation of a new boundary point. These three cases are handled as follows, see Fig. 2. When only one new immersed boundary point is created, we connect that point to the opposite vertex, as in the left panel of Fig. 2, thus partitioning the original triangle into two new triangles. When two new vertices are created, we connect them as shown by the solid line in the middle panel of Fig. 2. This cuts the original triangle into a triangle and a quadrilateral. The quadrilateral is further partitioned into two triangles by either of its diagonals (one of the two dashed lines in the middle panel of Fig. 2). We choose the shorter of the two diagonals for this purpose (unless the two diagonals are equal, in which case we choose either one arbitrarily). When three new vertices have been created, we simply form a new edge joining each pair of new vertices. This cuts the original triangle into four new triangles as shown in the right panel of Fig. 2. In all three cases, the sum of the areas of the new triangles is, of course, equal to the area of the original triangle. This means that the surface energy is not changed at all by the refinement process. Another important property of this refinement scheme is that it preserves the requirement that no vertex of a triangle is interior to the edge of any other triangle, i.e., if this requirement is met before refinement, it is met after refinement as well. The reason for this is simply that the starting point of the refinement process is to decide whether each edge is to be refined or not. If an edge is refined, both triangles which share that edge are refined accordingly.

Whenever $|\mathbf{X}_1 - \mathbf{X}_2| < h/5$, we delete both points (thus the edge between the points) and create in their place a new boundary point halfway between them. This deletes the edge that previously connected $\mathbf{X}_1$ and $\mathbf{X}_2$, and it also deletes the two triangles which previously shared that edge. Any edge, other than the deleted edge, which previously had a vertex at $\mathbf{X}_1$ or $\mathbf{X}_2$ is now considered to have that vertex replaced by the new vertex, the location of which is $(\mathbf{X}_1 + \mathbf{X}_2)/2$, see Fig. 3. Unlike the process of triangulation refinement discussed above, this procedure of triangulation coarsening does change the surface area (and hence the surface energy). Notice, too, that the coarsening algorithm is inherently sequential, and that the results may depend upon the order in which the edges are considered. To remove this arbitrariness, we order the edges by length, and delete the shortest edge first (if its length is less than $h/5$) and continue in this manner until all edges of length less than $h/5$ have been deleted. Edges that are not deleted may become longer or shorter during coarsening. This is ignored, however, until the next time step. Thus, in a given time step, edges are deleted or not deleted based on their length prior to the application of the coarsening process.
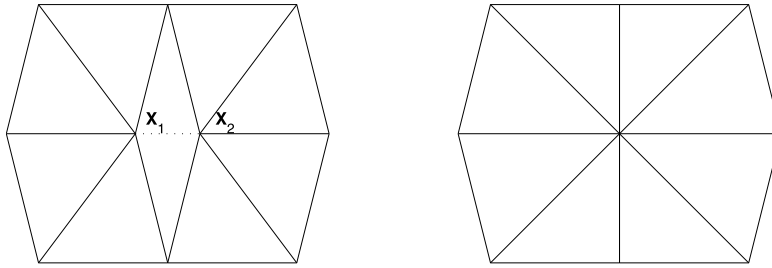
Fig. 3. Coarsening of edges and triangles. When the distance between two points $\mathbf{X}_1$ and $\mathbf{X}_2$ is less than $h/5$ (dotted line in the left panel), we delete both points and create in their place a new boundary point halfway between them. This deletes the edge that previously connected $\mathbf{X}_1$ and $\mathbf{X}_2$, and it also deletes the two triangles which previously shared that edge. Any edge, other than the deleted edge, which previously had a vertex at $\mathbf{X}_1$ or $\mathbf{X}_2$ is now considered to have that vertex replaced by the new vertex, the location of which is $(\mathbf{X}_1 + \mathbf{X}_2)/2$ (right).

3.2.3. Implementation of no-slip boundary conditions by applying a boundary feedback force

To complete the description of the numerical IB method, we need to explain the boundary conditions imposed over the surface of a fixed or moving wall. In this paper, we use a cylindrical surface as a wall which contains foams. We impose the no-slip condition over the boundary surface by laying out an array of "target points" along the boundary surface. Let $\mathbf{Y}(r, s, t)$ be the target points along the boundary, then the method used to impose no-slip condition is to apply to the boundary the following force:

$$\mathbf{F}_0(r, s, t) = c_0\big(\mathbf{Y}(r, s, t) - \mathbf{X}(r, s, t)\big), \tag{20}$$

where c_0 is a large constant and $\mathbf{X}(r, s, t)$ is immersed boundary point that moves at the local fluid velocity and applies $\mathbf{F}_0(r, s, t)$ locally to the fluid. This provides a feedback mechanism for computing the boundary force needed to enforce the no-slip condition. In the present paper, the target points $\mathbf{Y}(r, s, t)$ are fixed (i.e., independent of time) to simulate stationary walls, or they move in a prescribed manner to simulate a moving wall. Note that the target-point method for enforcing the no-slip condition still allows the use of FFT, since we do so not by changing the boundary conditions per se but instead by applying forces that effectively prevent the fluid from moving, or force it to move in a prescribed manner, at the specified locations.

4. Results and discussion

4.1. Initial setting

Consider a computational domain Ω filled with an incompressible fluid in which foam boundaries are immersed and divide the fluid into several bubbles, see Fig. 4. Throughout this paper, we fix the computational domain $\Omega = [-1, 1] \times [-1, 1] \times [-1, 1]$ mm^3, and the no-slip (rigid) boundary conditions are imposed along the circular cylinder $x^2 + y^2 = 1$ mm^2, unless otherwise stated. Note that the rigid cylinder extends from the top to the bottom of the periodic domain, and that its ends are open, i.e., there is no rigid wall on the top or on the bottom, so that the upper cell of the foam and the lower cell of the foam are actually parts of the same cell.

To impose the no-slip boundary conditions, we use the target-point idea described in the previous section (Eq. (20)) with

$$\mathbf{Y}(\theta, s, t) = (\cos\theta, \sin\theta, s), \tag{21}$$

where $0 \leqslant \theta \leqslant 2\pi$ and $-1 \leqslant s \leqslant 1$. In Eq. (20), we choose a value of c_0 by trial and error. As c_0 increases, a larger force is generated for any given displacement $\mathbf{Y}(\theta, s, t) - \mathbf{X}(\theta, s, t)$, and the computation may become unstable, in which case, we need to reduce the time step Δt. Our strategy is to choose an allowed distance between the target point $\mathbf{Y}$ and the immersed boundary point $\mathbf{X}$, to adjust c_0 until it is large enough that this allowed distance is not exceeded, and to reduce the time step Δt, if necessary, as c_0 is increased, to avoid numerical instability. The allowed distance is normally chosen to be one-tenth the meshwidth, i.e., $\|\mathbf{X} - \mathbf{Y}\|_\infty \leqslant h/10$. We have found that our simulations run stably whenever $\Delta t < 0.5/\sqrt{c_0}$ for different choices of c_0 ranging from 1.0×10^5 g/(cm s)^2 to 4.0×10^6 g/(cm s)^2, which agrees well with the stability constraint found in the virtual boundary method [20,21] to create no-slip boundary condition. Throughout this paper, we choose the stiffness number c_0 as 5×10^5 g/(cm s)^2.

For the initial configuration of the internal boundaries of the foam, we construct surfaces which are written as the following parametric equations:

$$\mathbf{X}_1(\theta, s) = \left(\frac{1}{2}\cos\theta, \frac{1}{2}\sin\theta, s\right), \quad 0 \leqslant \theta \leqslant 2\pi, \ -\frac{1}{2} \leqslant s \leqslant \frac{1}{2}, \tag{22}$$

$$\mathbf{X}_2(r, s) = \left(r, s, \pm\frac{1}{2}\right), \quad r^2 + s^2 \leqslant \frac{1}{4}, \tag{23}$$
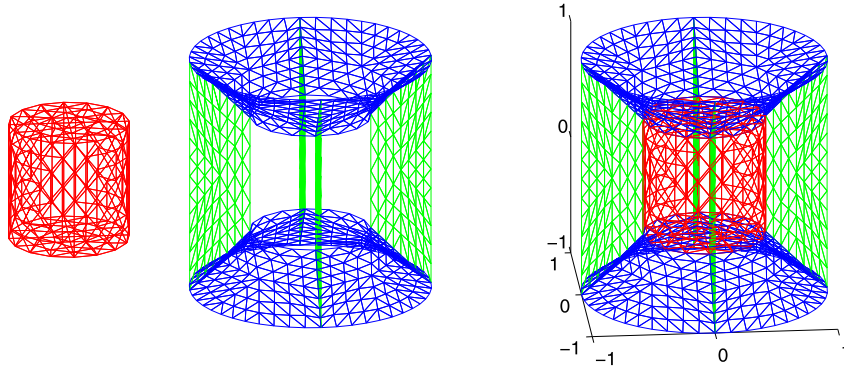
Fig. 4. Construction of an initial foam configuration. Left panel shows the "inner cell" of the foam (red), which is initially a circular cylinder with planar top and bottom. Middle panel shows $n = 4$ initially planar internal boundaries (green) of the foam that connect the inner cell to an outer rigid circular cylinder (not shown), and also two initially conical internal boundaries (blue) of the foam that connect the initially circular junction edges of the inner cell to the circular top and bottom of the outer rigid cylinder. The right panel shows all of the internal boundaries of the foam. In all three panels, the initial triangulation of the these internal boundaries is shown. The triangulation in the figure is the one that is used with a $16 \times 16 \times 16$ fluid grid, and is refined proportionally for use with finer grids. (For interpretation of the references to color in this figure legend, the reader is referred to the web version of this article.)

$$\mathbf{X}_3(r, s) = \left(\cos\left(\frac{2\pi}{n} i \right) r, \sin\left(\frac{2\pi}{n} i \right) r, rs \right), \quad \frac{1}{2} \leqslant r \leqslant 1, \; -1 \leqslant s \leqslant 1, \; i = 1, \ldots, n, \tag{24}$$

$$\mathbf{X}_4(\theta, s) = (s \cos\theta, s \sin\theta, \pm s), \quad 0 \leqslant \theta \leqslant 2\pi, \; \frac{1}{2} \leqslant s \leqslant 1. \tag{25}$$

The unit of length in Eqs. (21)–(25) is the millimeter (mm). The surface $\mathbf{X}_1$ is a circular cylinder with radius $1/2$ mm and height 1 mm, and the surface $\mathbf{X}_2$ is a pair of planes on the top and bottom of this cylinder. The region enclosed by the surfaces $\mathbf{X}_1$ and $\mathbf{X}_2$ will be called the inner cell of the foam, and is shown in the left panel of Fig. 4. The surfaces $\mathbf{X}_3$, which represent n radial planar boundaries, each with a trapezoidal profile, connect the inner cell to the outer rigid wall $\mathbf{Y}(\theta, s, t)$. This rigid wall is a circular cylinder of radius 1 mm. In our initial studies it is at rest, so that $\mathbf{Y}(\theta, s, t) = (\cos\theta, \sin\theta, s)$ for $0 \leqslant \theta \leqslant 2\pi$ and -1 mm $\leqslant s \leqslant 1$ mm. Later, we shall consider a moving wall, see Eq. (28).

The surface $\mathbf{X}_4$ with positive (and negative) sign connects the boundaries of the surface $\mathbf{X}_2$ with positive (and negative) sign, the radial planes $\mathbf{X}_3$, and the outer rigid wall $\mathbf{Y}$, see the middle panel of Fig. 4. These surfaces together form the internal boundaries of the foam, and their intersection curves are Plateau borders (triple junctions), see the right panel of Fig. 4.

From this particular way of constructing the internal foam boundaries, the inner cell is initially a circular cylinder with top and bottom boundary faces. Since it has n triple junctions (edges) on its side and n triple junctions along the circular boundaries of both top and bottom faces, the inner cell has $3n$ edges and $n + 2$ faces (n faces on its side and 2 faces on its bottom and top boundaries). Since there exists a neighboring cell on each of $n + 1$ faces of the inner cell, the total number of cells (bubbles) is $n + 3$. The right panel of Fig. 4 shows the initial configuration of a foam with $n = 4$, and we shall later change the number n for comparison.

The mesh width of the computational domain, $h = \Delta x = \Delta y = \Delta z = 2/64$ mm, is uniform and fixed in time, and the time step duration is $\Delta t = 5 \times 10^{-4}$ ms. The fluid density is $\rho = 1.2 \times 10^{-3}$ g/cm^3, and the viscosity is $\mu = 1.8 \times 10^{-4}$ g/(cm s). These values are the same as those of air. The surface tension γ used in Eq. (9) is fixed at 25.0 erg/cm^2. Since each soap film of the foam actually has two gas–liquid interfaces, one on each side of the film, this means that we are assuming a surface tension of 12.5 erg/cm^2 for each interface between the soap solution and air. We use two different permeabilities, $M = 0$ and 0.002 cm^3/(dyne s), to see how the permeability affects the foam dynamics.

4.2. Convergence study

In order to provide verification that the present IB method correctly solves the foam dynamics, we perform a convergence study. We consider a foam with a single inner cell which was constructed above with $n = 4$, see Fig. 4. The "inner cell" is the one in the center of the foam. It is initially cylindrical and is shown by itself in the left-hand panel of Fig. 4, and is shown together with the other foam boundaries in the right-hand panel of that figure. We choose two different permeabilities: $M = 0$ and 0.002 cm^3/(dyne s). Fig. 5 shows the motion of the inner cells of these two computations at some selected times: 8 ms, 24 ms, and 40 ms from left to right. Independent of the permeability, there is a rapid transient at the beginning of the computation, since we have started in a non-equilibrium configuration. In particular, the dihedral angles of our initial foam configuration are not equal to $\pi/3$, and this implies a nonzero net surface tension force per unit length concentrated along each Plateau border. The shape of the inner cell following this transient is seen in the upper row of Fig. 5, which depicts the case of zero permeability ($M = 0$). Note that both the volume and shape of the inner cell
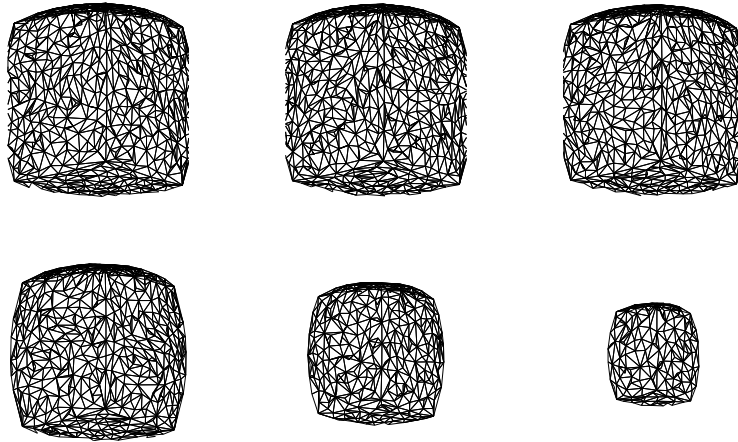
Fig. 5. Motion of the inner cell (in the left panel of Fig. 4) at some selected times: 8 ms, 24 ms, and 40 ms from left to right. The permeability is $M = 0$ on the top and $M = 0.002$ cm^3/(dyne s) on the bottom. The inner cell in both cases initially changes its shape to reach the spherical surfaces, after which, whereas the inner cell with the permeability $M = 0$ maintains its shape and volume (top), the inner cell with a positive permeability decreases its volume (bottom).
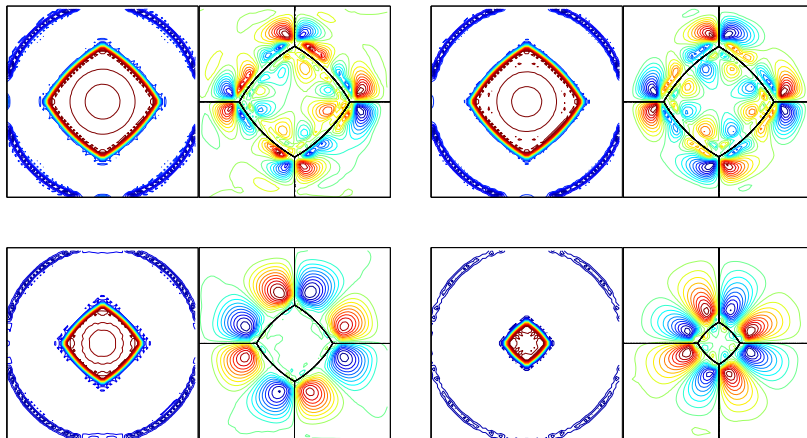
Fig. 6. Pressure contours (left panel of each pair of figures) and streamlines (right panel of each pair of figures) of the components u and v of the velocity fields on the middle horizontal plane $z = 0$. The permeability is $M = 0$ (top panels) and $M = 0.002$ cm^3/(dyne s) (bottom panels), and the times are 24 ms (left pairs) and 40 ms (right pairs). (For interpretation of the references to color in this figure, the reader is referred to the web version of this article.)

quickly become stationary in this case. In the case of positive permeability ($M = 0.002$ cm^3/(dyne s)), the initial transient described above is followed by a phase in which the inner cell of the foam slowly loses volume to the other cells (lower row of Fig. 5).

Since our computation is based on fluid mechanics, we can obtain the fluid velocity field as well as the motion of the internal boundaries of a foam. Fig. 6 shows the pressure contours on the left panel of each pair of figures and streamlines of the x and y components u and v of the velocity field on the right panel of each pair of figures. The permeability is $M = 0$ (top panels) and $M = 0.002$ cm^3/(dyne s) (bottom panels). The times are 24 ms (left pairs) and 40 ms (right pairs). The pressure and the velocity field (u, v) are taken in the middle horizontal plane $z = 0$. We can see that the pressure inside the inner cell (red color) is bigger than that outside the inner cell (blue color) independent of the permeability. Note that, when the permeability is positive, the volume of the inner cell decreases as time evolves so that the mean curvature of the inner cell increases accordingly. Thus the pressure difference between the interior and exterior of the cell increases as time goes on. The outer circles in blue color indicate the no-slip boundary.

Since the velocity field (u, v) is not generally divergence-free, in order to avoid the path dependency of the streamlines, we project (u, v) onto the space of divergence-free vector fields in the following way; we first solve the equation $\Delta \psi = \frac{\partial u}{\partial y} - \frac{\partial v}{\partial x}$, and then set $(U, V) = (\frac{\partial \psi}{\partial y}, -\frac{\partial \psi}{\partial x})$. Note that (U, V) is now divergence-free, and that we have checked that the velocity field (u, v) is close to (U, V). Thus it is reasonable to draw the streamlines of (U, V) in Fig. 6 instead of those of (u, v). We can observe that, when the permeability is zero, the clockwise (or counter-clockwise) flows in the neighboring region outside the inner cell are compensated by the opposite flows in the neighboring region inside the inner cell, and
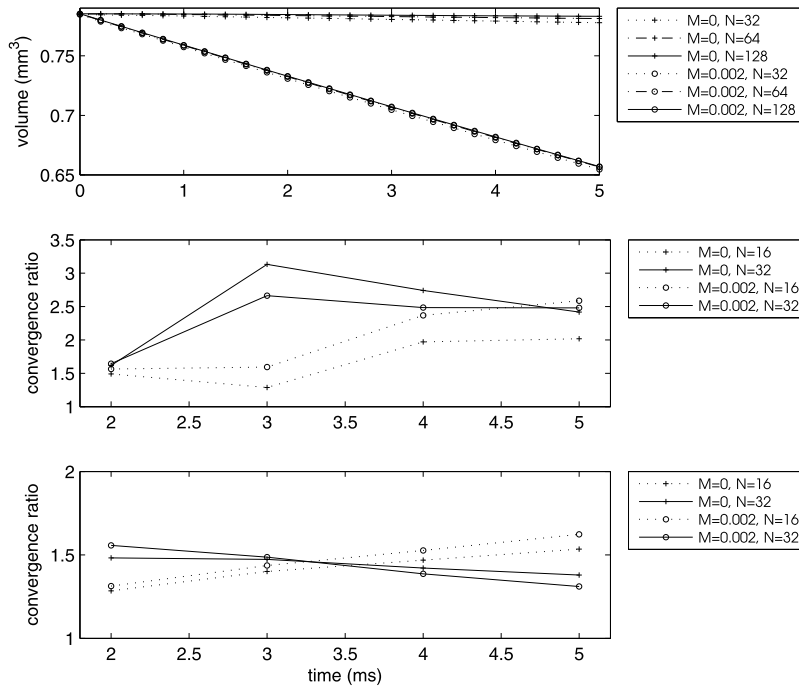
Fig. 7. The top panel shows the volume change of the inner cell in terms of time for each of the three mesh sizes ($N = 32$, 64, and 128) and the two permeabilities ($M = 0$ and 0.002 cm^3/(dyne s)), and the middle and bottom panels show the convergence ratios of the computed velocity field $\mathbf{u}(\mathbf{x}, t)$ and pressure $p(\mathbf{x}, t)$ of the fluid, respectively, for each of the two mesh sizes ($N = 16$ and 32) and the two permeabilities ($M = 0$ and 0.002 cm^3/(dyne s)). The convergence ratios for the velocity are near two (first order accuracy), and those for the pressure are around 1.3–1.5 (half-order accuracy).

thus the inner cell almost does not move. In the case of positive permeability, the triple junctions are moving outward, but the inward motion of the centers of the edges (faces in 3D) enforces the inner cell as a whole to collapse inwards.

Now we choose the mesh sizes of the domain $N = 16$, 32, 64, and 128 so that the corresponding mesh width is $h = 2/N$ mm. We also choose Δt proportional to h, so that the factor of two in refinement of the fluid mesh width is accompanied by the same factor of refinement for the time step duration. When we refine both h and Δt, the triangles representing the internal boundary surfaces of the foam are also refined by connecting the middle points of each edge of the triangles. This refinement of triangulation replaces one triangle by four triangles as illustrated in the right panel of Fig. 2 and induces almost the same factor of refinement for the boundary mesh as those for the fluid mesh width and the time step duration.

The top panel of Fig. 7 shows the volume of the inner cell as a function of time for each of the three mesh sizes ($N = 32$, 64, and 128) and the two permeabilities ($M = 0$ and 0.002 cm^3/(dyne s)). We can see that, whereas the volume of the inner cell with $M = 0$ is almost a constant in time, the inner cell volume with a positive permeability decreases almost linearly. Note that there is a slight volume loss even with $M = 0$. The volume loss is typical in the IB computations, and here we use a special recipe in [13,16] of the IB computation to have a better volume-preserving property. We can also observe that, for each permeability, the volume changes in time for the three cases of N's are in good agreement. Especially, when $M = 0.002$ cm^3/(dyne s), the difference of the volume changes between the cases of $N = 64$ and 128 is smaller than that between the cases of $N = 32$ and 64, which suggests the convergence of the solutions.

To get a more quantitative measure of convergence, we compare the velocity fields computed on the three different meshwidths. Fig. 7 shows the convergence ratios of the computed fluid velocity $\mathbf{u}(\mathbf{x}, t)$. Since we do not know the exact solution of the problem, the estimation of the convergence ratio requires three numerical solutions for three consecutive N's. Let (u_N, v_N, w_N) be the velocity field, and let $\| \cdot \|_2$ be L_2 norm. The middle panel of Fig. 7 shows the convergence ratios $(\|u_N - u_{2N}\|_2^2 + \|v_N - v_{2N}\|_2^2 + \|w_N - w_{2N}\|_2^2)^{1/2}/(\|u_{2N} - u_{4N}\|_2^2 + \|v_{2N} - v_{4N}\|_2^2 + \|w_{2N} - w_{4N}\|_2^2)^{1/2}$ versus time for each of the two mesh sizes ($N = 16$ and 32) and the two permeabilities ($M = 0$ and 0.002 cm^3/(dyne s)). The bottom panel shows the corresponding convergence ratios for the pressure $p(\mathbf{x}, t)$ which are computed in a similar manner to those of the fluid velocity.

One can see from the figure that the convergence ratios for the fluid velocity are around two, which indicates that the present method is first-order accurate. However, the convergence ratios for the pressure are around 1.3–1.5, which implies half-order accuracy. This is the typical behavior in accuracy for the IB method as applied to problems with thin elastic boundaries in which the pressure has jump discontinuity along the immersed boundary [22]. For second order IB method in the case of an immersed elastic structure of finite thickness, the interested readers can refer to [23,24].
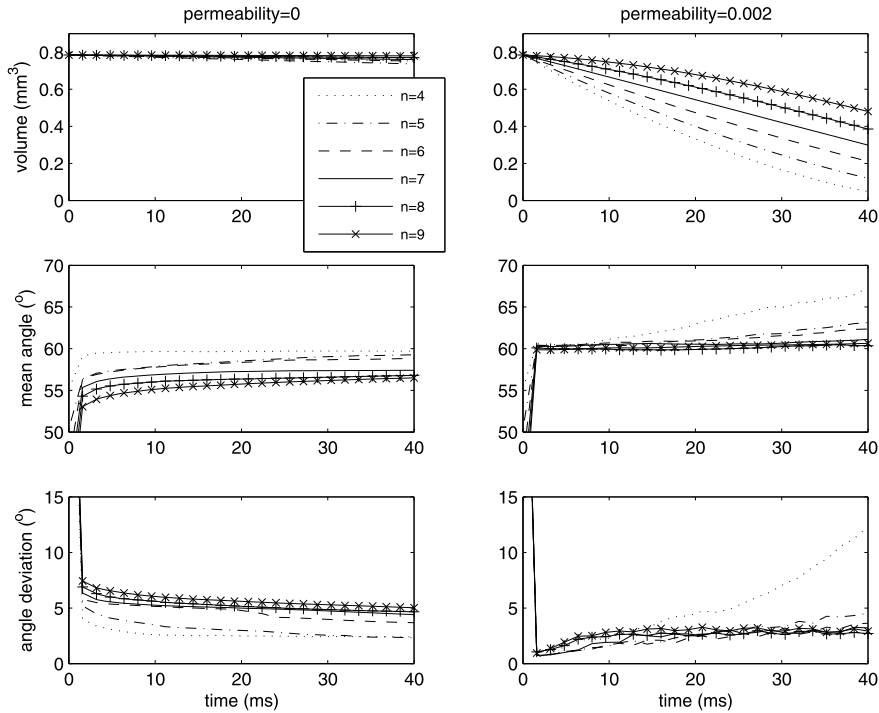
Fig. 8. The volume of the inner cell (top panels), the mean dihedral angle at the triple junctions (middle panels), and the root-mean-square deviation of the dihedral angles (bottom panels) as functions of time for the two permeability parameters: $M = 0$ (left panels) and $M = 0.002$ cm^3/(dyne s) (right panels).

4.3. Numerical verification of discretized 3D von Neumann relation

In order to verify the discrete version of 3D von Neumann relation (3), we consider two different permeability parameters $M = 0$ and $M = 0.002$ cm^3/(dyne s), and several different inner cells with the number of the radial planes in the construction described above varying from $n = 4$ to $n = 9$. The top panels of Fig. 8 plot the volume of the inner cell as functions of time for the two permeability parameters: $M = 0$ (left) and $M = 0.002$ cm^3/(dyne s) (right). When there is no permeability ($M = 0$), since the fluid is incompressible, the volume of the inner cells does not change for all n's. When the permeability is positive, the volume of the inner cells decreases for all n's with decrement being slower as n increases. Note that the volume here is not a linear function of time, as the area is in the 2D case according to the 2D von Neumann relation (1).

The derivation of the 3D generalized von Neumann relation in [4] is based on the assumption that the boundary surfaces of a cell meet along junction edges with dihedral angles equal to $\pi/3$ measured in the plane perpendicular to the edges. The middle panels of Fig. 8 show the mean angle of the computed angles along the junction edges of the inner cell, and the bottom panels show the root-mean-square deviation of the computed angle from the mean angle. The mean angle $\bar{\theta}$ and the root-mean-square deviation $rms(\bar{\theta})$ are computed by the following two equations, respectively:

$$\bar{\theta} = \frac{1}{L} \sum_{i=1}^{v} \theta_i L_i; \qquad rms(\bar{\theta}) = \sqrt{\frac{1}{L} \sum_{i=1}^{v} (\theta_i - \bar{\theta})^2 L_i}, \tag{26}$$

where L_i is the length of edge i of the triangular facets which constitutes the junction edge, and θ_i is the exterior (turning) angle between the two facets which share the edge i along the junction. The total length of the junction of the inner cell is L, i.e., $L = \sum_{i=1}^{v} L_i$. We can see from the figure that the mean dihedral angles over the triple junctions are around $\pi/3$ (60 in degrees) and their angle deviations are small in both impermeable and permeable cases. This implies that the assumption that the boundaries of the surfaces meet along junction edges with dihedral exterior angle $\pi/3$ is correctly imposed in the 3D generalized von Neumann relation in [4].

Unlike the 2D von Neumann relation (1), in which the rate of change of the area of a given cell (a curved polygon) is solely dependent on the number of walls, the 3D von Neumann relation (3) is not topological. The rate of change of volume of a given cell (a curved polyhedron) in a three-dimensional dry foam is dependent on the cell size in some way as well as on the number of faces of the cell. Since the size of the cell changes as time goes on, the rate of change of its volume also changes, and thus we need to check the discretized 3D von Neumann relation (3) at each time step.
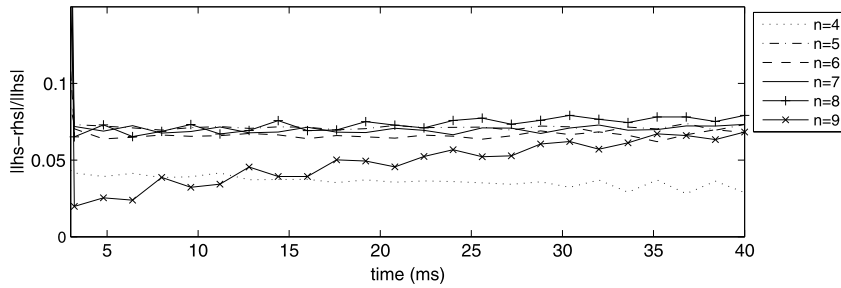
Fig. 9. Graphs of $|lhs - rhs|/|lhs|$ in terms of time where *lhs* and *rhs* are defined in Eq. (27). The right- and left-hand sides of (27) are very close, which confirms the 3D generalized von Neumann relation (3) and thus (2) approximately.

We here verify numerically the discrete version of the von Neumann relation (3) at each time step. To do that, we record the volume $V(t)$ of the given inner cell, the length $L_e(t)$ of the edge e of all triangular facets, and the exterior (turning) angle $\theta_e(t)$ at the edge e at time level t. Then the time discretization of Eq. (3) gives the following discretized equation:

$$\frac{V(t + \Delta t) - V(t)}{\Delta t} = -M\gamma \sum_{e \in E_0} L_e(t)\theta_e(t) - \frac{M\gamma}{2} \sum_{e \in E_1} L_e(t)\theta_e(t). \tag{27}$$

Let the left and right-hand sides of (27) be denoted by *lhs* and *rhs*, respectively. Fig. 9 shows the relative error $|lhs - rhs|/|lhs|$ in terms of time. The inner foam has the number of radial planes varying from $n = 4$ to $n = 9$, and the permeability parameter is $M = 0.002$ cm^3/(dyne s). One can see that the relative difference between the right- and left-hand sides of Eq. (27) are very small, which confirms the discretized 3D von Neumann relation (3).

4.4. Dynamic flow

The fluid dynamics of a foam is not necessarily restricted to the slow coarsening regime that has been considered up to now. To illustrate this, we use the same initial configuration of the foam as in Fig. 4 in which we have used no-slip (rigid) wall along the outer circular cylinder represented as $\mathbf{Y}(\theta, s, t) = (\cos\theta, \sin\theta, s)$, where $0 \leqslant \theta \leqslant 2\pi$ and $-1 \leqslant s \leqslant 1$. Instead of using a fixed wall, we create target points which rotate on the rigid wall in an oscillatory manner. This motion of the target points can be created by defining the time-dependent surface as

$$\mathbf{Y}(\theta, s, t) = \left(\cos\left(\theta + \tilde{\theta}(t)\right), \sin\left(\theta + \tilde{\theta}(t)\right), s\right), \tag{28}$$

where $\tilde{\theta}(t) = A\sin(2\pi\omega t)$. The target points on the circular cylinder rotate right and left with the amplitude $A = \pi/4$ and the frequency $\omega = 25$. We call the resulting motion a *dynamic flow* and refer to the special case $A = 0$ as a *stationary flow*.

Fig. 10 shows the streamlines of the velocity field (u, v) projected onto the space of divergence-free vector fields as in Fig. 6. The foam has the number of radial planes $n = 6$ in three different situations: zero permeability in a stationary flow (left), $M = 0.002$ cm^3/(dyne s) in a stationary flow (middle), and $M = 0.002$ cm^3/(dyne s) in a dynamic flow (right). The times are $t = 24$ ms (top) and 40 ms (bottom). We can observe the rotating flows in the main flow region between the foam boundaries which also rotates in the dynamic flow case. Whereas the inner cell almost does not change when the permeability is zero (left), the inner cells shrink over time both in the stationary and in the dynamic case when the permeability is positive (middle and right).

We can see from Fig. 10 that, even though the foam is now far from equilibrium, the volume of the inner cell still decreases when there is a positive permeability. Fig. 11 shows the volume change of the inner cell (upper-left), the mean dihedral angle along the junction edges of the inner cell (upper-right), the root-mean-square deviation from the mean dihedral angle (lower-left), and $|lhs - rhs|/|lhs|$ in terms of time where *lhs* and *rhs* are defined in (27) (lower-right). The number of radial planes of the inner cell varies from $n = 4$ to $n = 9$, and the permeability is fixed at $M = 0.002$ cm^3/(dyne s). We can see that the volume changes of the inner cells in this dynamic flow is almost the same as those in the stationary flow, compare Figs. 8 and 11. We also find that, even though the foam interacts with a dynamic flow, the dihedral (exterior) angle along the triple junctions is around $\pi/3$ (60 in degrees) as imposed in the theory of the 3D von Neumann relation. The lower-left panel shows that the right- and left-hand sides of (27) are very close, which verifies the discretized 3D von Neumann relation (3).

4.5. A foam with multiple cells

Finally, we consider a foam with a more general configuration. Although we use the same computational domain $\Omega = [-1, 1] \times [-1, 1] \times [-1, 1]$ mm^3, here we use periodic boundary conditions without any rigid wall. We construct a Voronoi diagram to set up an initial configuration of a foam [6,7]. To do that, we first choose randomly a set of points in Ω which will sit inside each cell of a foam. In order to take the periodicity into account, we extend the domain into a cube
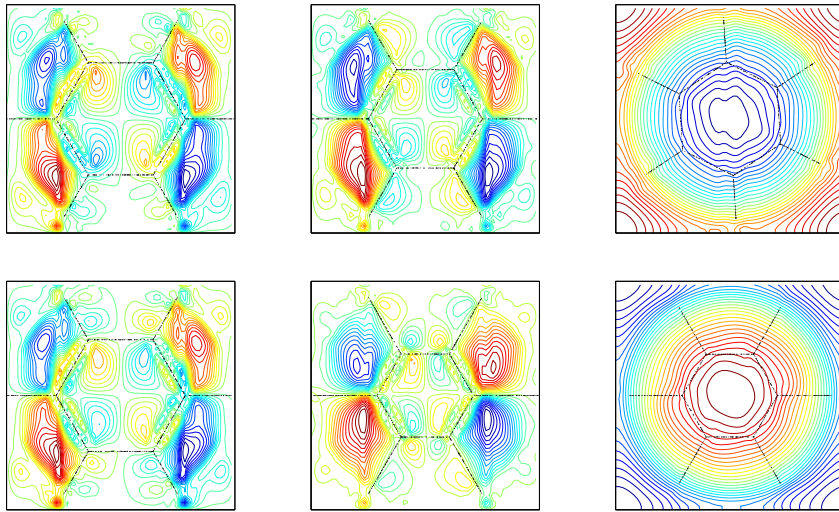
Fig. 10. The streamlines of the velocity field (x and y components only) of the foam which has the number of radial planes $n = 6$ for three different cases: zero permeability in a stationary flow (left), $M = 0.002$ cm^3/(dyne s) in a stationary flow (middle), and $M = 0.002$ cm^3/(dyne s) in a dynamic flow (right). The velocity field is taken in the horizontal plane $z = 0$, and the times are $t = 24$ ms (top) and 40 ms (bottom).
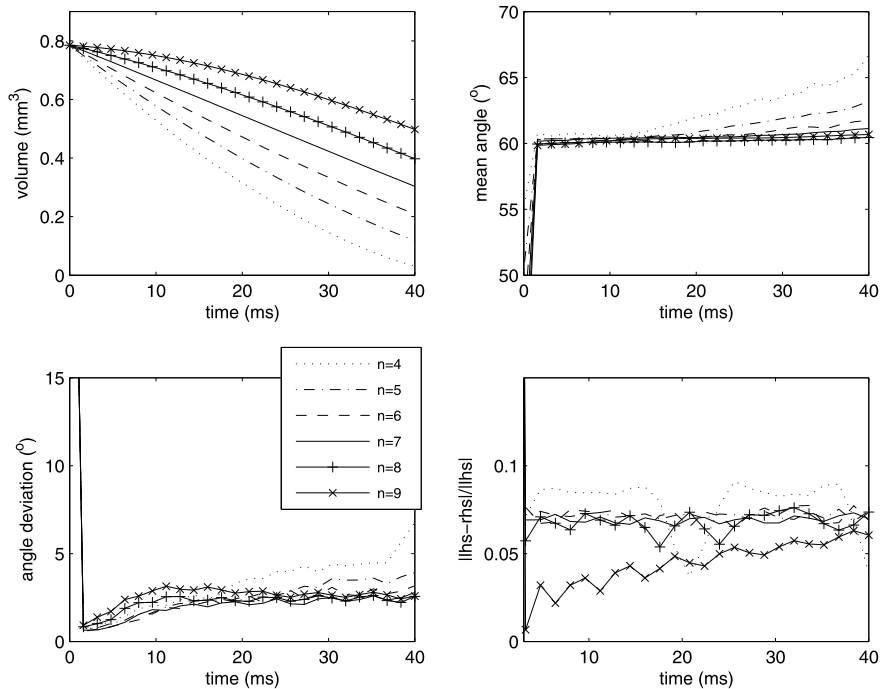
Fig. 11. Volume change of the inner cell (upper-left), the mean dihedral angle along the junction edges of the inner cell (upper-right), the root-mean-square deviation from the mean dihedral angle (lower-left), and $|lhs - rhs|/|lhs|$ in terms of time where lhs and rhs are defined in (27) (lower-right). The number of radial planes of the inner cell varies from $n = 4$ to $n = 9$, and the permeability is fixed at $M = 0.002$ cm^3/(dyne s). Even though the foam is far from equilibrium, these figures are quite comparable to Figs. 8 and 9 obtained in the case of the stationary flow.

$[-3, 3] \times [-3, 3] \times [-3, 3]$ mm^3 and copy the set of points chosen in Ω periodically into the extended cube. Then we construct a Voronoi network using the set of points which is obtained by using 'Voro++' [25], an open source software library for carrying out 3D cell-based Voronoi tessellations. Now we consider only the cube Ω as the computational domain in which a network of foam boundaries exists periodically, see the left panel of Fig. 12 which shows the initial configuration of a general foam with 40 cells. The right panel is a histogram showing the number of cells in the foam that have each of the different numbers of faces that actually occur in the foam. For example, only one cell of the foam has 10 faces, 6 cells have 14 faces, and 3 cells have 22 faces, etc.
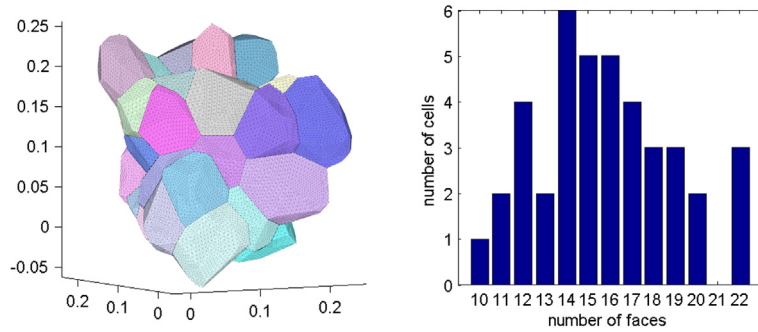
Fig. 12. The initial configuration of a general foam (left) and a histogram (right) showing the number of cells in the foam that have each of the different numbers of faces that actually occur in the foam (which vary from a minimum of 10 faces to a maximum of 22 faces). The configuration shown in the left panel was constructed by Voronoi tessellation of a periodic domain.
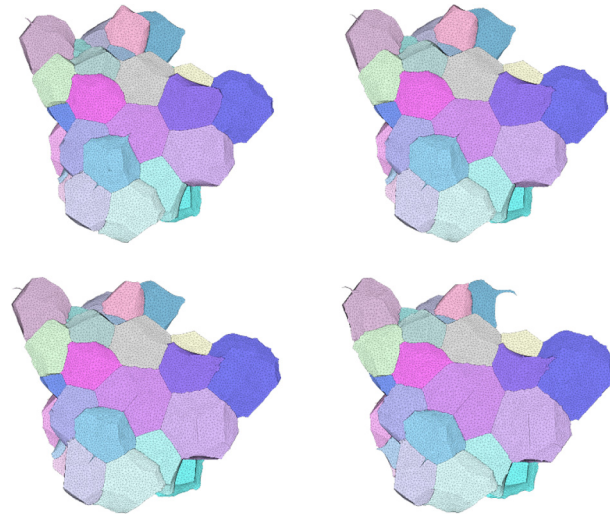
Fig. 13. The configuration of a general foam at some chosen times; $t = 9.6$ ms (upper-left), 19.2 ms (upper-right), 28.8 ms (lower-left), and 38.4 ms (lower-right).

Fig. 13 shows the configuration of the general foam at some chosen times; $t = 9.6$ ms (upper-left), 19.2 ms (upper-right), 28.8 ms (lower-left), and 38.4 ms (lower-right). Although the foam boundaries are initially composed of planar faces as shown in Fig. 12, they immediately evolve into curved shapes. An online animation for the 3D foam is available on the web: http://cau.ac.kr/~kimy/Movie/movie_V40.gif.

The top panel of Fig. 14 shows the motion of four selected cells in time. The yellow cell at the lower-right has 11 faces, the green cell at the lower-left has 15 faces, the blue cell at the upper-left has 18 faces, and the red cell at the upper-right has 22 faces. The figure shows the motion of these cells at three chosen times: $t = 0$, 12 ms, and 24 ms from left to right. Note that the cells with 11 and 15 faces lose their volumes over time, whereas the cells with 18 and 22 faces gain their volumes. The lower-left panel of Fig. 14 shows the volume change in time relative to the initial volume of each of the four selected cells. Again, while the volumes of cells with 11 and 15 faces decrease with the decrement being faster for the 11-faced cell, those of cells with 18 and 22 faces increase with the increment being faster for the 22-faced cell. The bottom-right panel plots the function $|lhs - rhs|/|lhs|$ in terms of time where lhs and rhs are defined in (27) and shows that the relative differences between the right and left-hand sides of (27) are small for the four selected cells, which confirms the discretized 3D von Neumann relation (3).

According to the 2D von Neumann relation (1), cells with fewer than 6 sides tend to shrink, and that cells with more than 6 sides tend to grow; hence the "coarsening" of the foam, in which cells with large numbers of sides grow at the expense of cells with small numbers of sides. However, 3D foam does not have such a simple coarsening behavior. This is because, unlike the 2D von Neumann relation, the 3D von Neumann relation (both Eq. (3) and formula in [4]) is not topological, i.e., the volume change of a given cell depends on the geometric properties such as edge lengths and exterior angles in (3) and the mean width of the cell domain in [4]. Even though Fig. 14 showed that cells with small number of faces tend to shrink and cells with large number of faces tend to grow, we found that the volume change of some cells is not monotonically decreasing or increasing in time.
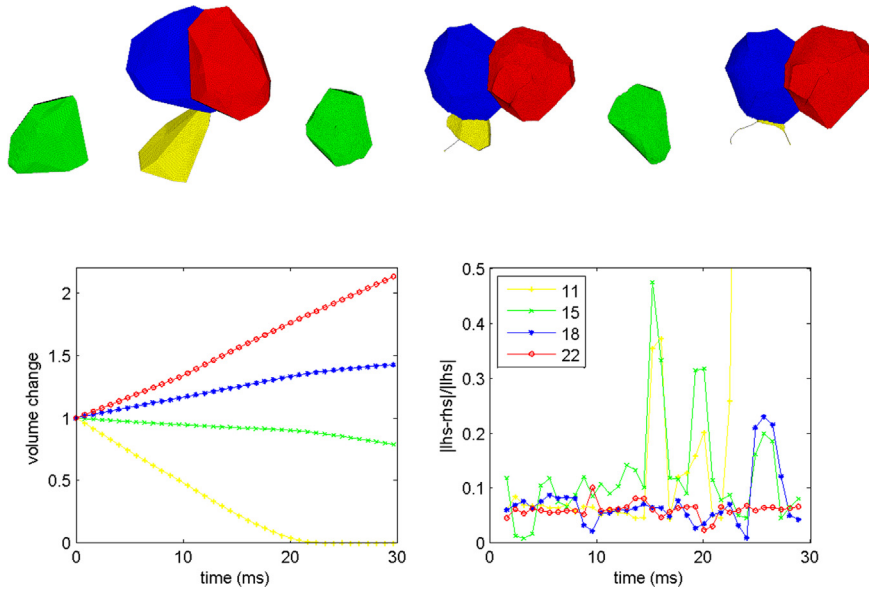
Fig. 14. Top: motion of cells with 11 faces (yellow one at the lower-right), 15 faces (green one at the lower-left), 18 faces (blue one at the upper-left), and 22 faces (red one at the upper-right) at some chosen times: $t = 0$, 12, and 24 from left to right. Bottom-left: volume change in time relative to the initial volumes of each of the four cells. Bottom-right: graph of $|lhs - rhs|/|lhs|$ in terms of time where *lhs* and *rhs* are defined in (27). (For interpretation of the references to color in this figure legend, the reader is referred to the web version of this article.)
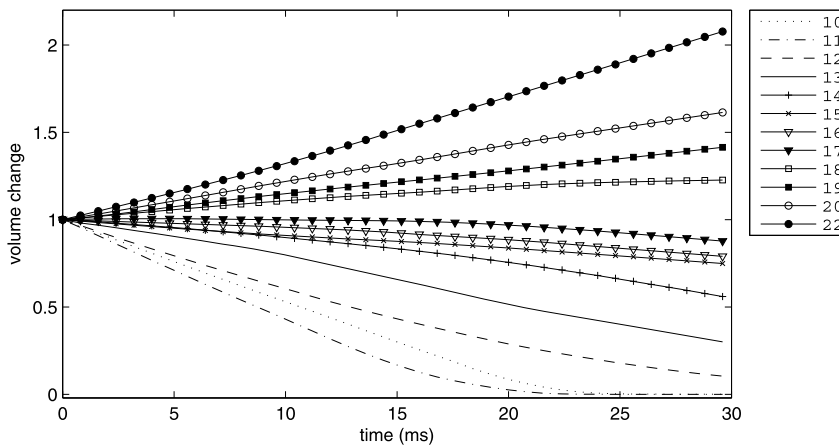
Fig. 15. The volume changes for all the cells in the foam as functions of time. The volume changes are averaged over cells with the same numbers of faces.

Fig. 15 plots the volume changes of all the cells of the foam as functions of time. The volume changes are averaged over cells with the same numbers of faces, for example, the volume of the 22-faced cell is averaged over the three 22-faced cells, see the right panel of Fig. 12. While the volume of the cells with the number of faces less than 18 decreases, the volume of the cells with larger number of faces (from 18) increases. Even though the volume changes of the cells are not linear functions of time as suggested in the 2D von Neumann relation, the overall volume changes in this 3D foam dynamics are comparable to the 2D case [13] and demonstrate the coarsening behavior of a foam structure, in which cells with large numbers of faces grow at the expense of cells with small numbers of faces.

There have been many researches to find the volume change of F-faced cells, and, analogous to the 2D von Neumann relation, it has been found that a 3D foam dynamics follows $V_F^{-1/3} \frac{dV_F}{dt} = \kappa(F - F_0)$, where V_F is the volume of a cell with F faces, and F_0 and κ are constants [26–29]. Note that V_F can be considered as the volume averaged over cells with the F faces. The constant F_0, which represents the face number of cells which do not change their volume in time, is found to be 13.4 in [28], 15.8 ± 0.1 in [26,27], and 17 ± 0.2 in [29]. Our simulation result shown in Fig. 15 suggests that F_0 is around 18. When we use different initial configurations of 3D foam of which the distributions of the number of cells versus the number of faces are shown in the left panels of Fig. 16, our simulation results give F_0 which is between 17 and 19 (see the right panels of Fig. 16). These values are slightly larger than F_0 given in [26–29].
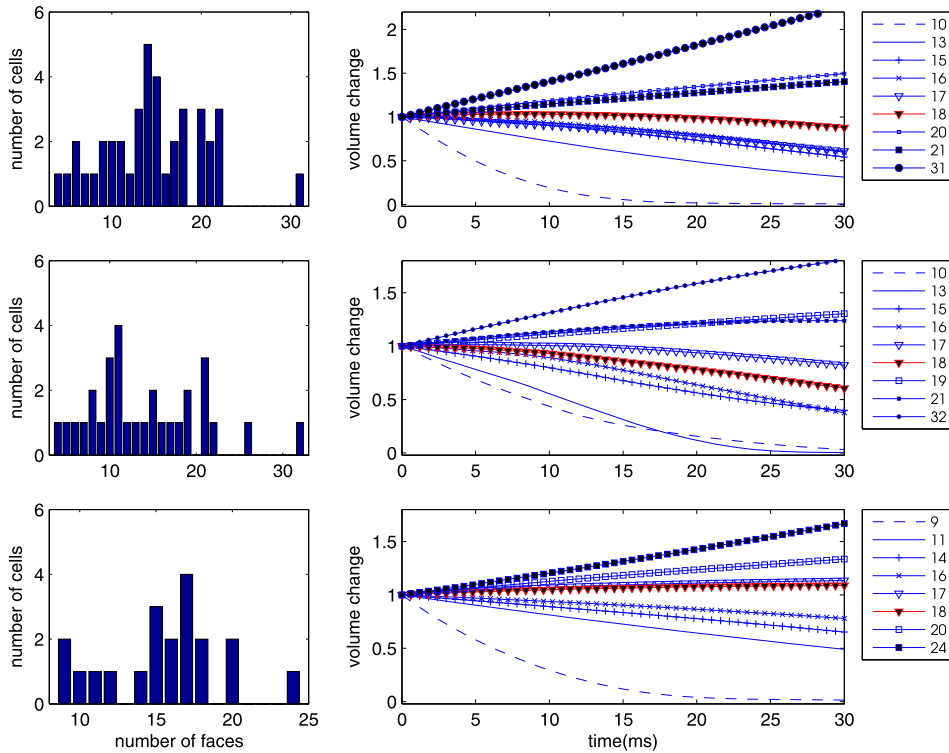
Fig. 16. The volume changes for the cells in the three different foams as functions of time. The volume changes are averaged over cells with the same numbers of faces. The left panels show the initial distribution of the number of cells versus the number of faces. The right panels show that the variation from the decrease to the increase of the cell volume occurs when the face number is between 17 and 19, i.e., $F_0 = 18 \pm 1$.

The discrepancy between our simulation results here and the literature might result from the fact that the foams used in our simulations are composed of only a small number of cells and that our model for the foam dynamics does not include any topological changes which allow for a steady scaling state [29,30]. In the scaling state, the average number of faces of the cells is around 13.5, and the distribution of the number of faces versus the number of cells is approximately of a bell-shape with its peak around at 13.5. However, since there is no topological change in the present model, the average number of faces, which is initially from 14.5 to 15.8, is constant in time. In order to study the statistical behavior of a dry 3D foam such as the volume change of the cells and the average number of faces in a scaling state, we need to extend our present method to simulate a 3D foam with a large number of cells and to include topological changes of a foam structure. This will be our future work.

5. Summary and conclusions

We have presented an immersed boundary method to simulate the fluid dynamics of a three-dimensional dry foam. We model the gas phase of the foam as a viscous incompressible fluid, and the liquid phase as a massless network of permeable internal boundaries under surface tension. The internal boundary force, generated by the surface tension, is everywhere normal to the internal boundaries. Permeability is modeled by allowing the internal boundaries to slip relative to the fluid, at a velocity (speed *and* direction) proportional to the boundary force. This is equivalent to slip in the normal direction only at a speed proportional to the pressure difference across each internal boundary, and thus models correctly the diffusion of gas through the liquid phase of the foam.

We have validated the method by doing a convergence study, which confirms the expected first-order accuracy of the scheme. Additional validation has been provided by showing numerically that the discretized 3D von Neumann relation is satisfied. We have also considered more complicated cases: one is the case in which non-equilibrium flows of gas occur within each cell of the foam, thus requiring the full fluid dynamics treatment of the present paper, and the other case is the foam of a general configuration.

Within the context of three-dimensional foams, the principal limitation of the method as currently implemented is that we do not allow for the resolution of quadruple or higher order junction edges into triple junction edges. (See [15] for a method that does allow topological changes in the 2D case.) More detailed investigation on the coarsening involving these topological changes will be the future work.

Appendix A. Derivation of force density

We here derive the force density $\mathbf{F}$ in Eq. (10) used in the model which is the variational derivative of the energy functional in Eq. (9):

$$E[\mathbf{X}] = \gamma \int |\mathbf{X}_r \times \mathbf{X}_s| \, dr \, ds, \tag{29}$$

where $X(r, s)$ is a parameterized surface and $\mathbf{X}_r = \frac{\partial \mathbf{X}}{\partial r}$ and $\mathbf{X}_s = \frac{\partial \mathbf{X}}{\partial s}$. Let $\mathbf{X} + \epsilon \mathbf{Y}$ be a perturbation of $\mathbf{X}$, then the variational derivative of $E[\mathbf{X}]$ is defined and can be calculated as follows:

$$
\begin{aligned}
\int \frac{\partial E}{\partial \mathbf{X}}(r, s) \cdot \mathbf{Y}(r, s) \, dr \, ds &= \lim_{\epsilon \to 0} \frac{E[\mathbf{X} + \epsilon \mathbf{Y}] - E[\mathbf{X}]}{\epsilon} \\
&= \lim_{\epsilon \to 0} \gamma \int \frac{|(\mathbf{X}_r + \epsilon \mathbf{Y}_r) \times (\mathbf{X}_s + \epsilon \mathbf{Y}_s)| - |\mathbf{X}_r \times \mathbf{X}_s|}{\epsilon} \, dr \, ds \\
&= \lim_{\epsilon \to 0} \gamma \int \frac{|(\mathbf{X}_r + \epsilon \mathbf{Y}_r) \times (\mathbf{X}_s + \epsilon \mathbf{Y}_s)|^2 - |\mathbf{X}_r \times \mathbf{X}_s|^2}{\epsilon (|(\mathbf{X}_r + \epsilon \mathbf{Y}_r) \times (\mathbf{X}_s + \epsilon \mathbf{Y}_s)| + |\mathbf{X}_r \times \mathbf{X}_s|)} \, dr \, ds \\
&= \lim_{\epsilon \to 0} \gamma \int \frac{2\epsilon (\mathbf{Y}_r \times \mathbf{X}_s + \mathbf{X}_r \times \mathbf{Y}_s) \cdot (\mathbf{X}_r \times \mathbf{X}_s) + O(\epsilon^2)}{\epsilon (|(\mathbf{X}_r + \epsilon \mathbf{Y}_r) \times (\mathbf{X}_s + \epsilon \mathbf{Y}_s)| + |\mathbf{X}_r \times \mathbf{X}_s|)} \, dr \, ds \\
&= \gamma \int \frac{(\mathbf{Y}_r \times \mathbf{X}_s + \mathbf{X}_r \times \mathbf{Y}_s) \cdot (\mathbf{X}_r \times \mathbf{X}_s)}{|\mathbf{X}_r \times \mathbf{X}_s|} \, dr \, ds \\
&= \gamma \int (\mathbf{Y}_r \times \mathbf{X}_s + \mathbf{X}_r \times \mathbf{Y}_s) \cdot \mathbf{n} \, dr \, ds \\
&= \gamma \int \left((\mathbf{X}_s \times \mathbf{n}) \cdot \mathbf{Y}_r + (\mathbf{n} \times \mathbf{X}_r) \cdot \mathbf{Y}_s \right) dr \, ds \\
&= -\gamma \int \left((\mathbf{X}_s \times \mathbf{n})_r + (\mathbf{n} \times \mathbf{X}_r)_s \right) \cdot \mathbf{Y} \, dr \, ds. \tag{30}
\end{aligned}
$$

Here $\mathbf{n} = (\mathbf{X}_r \times \mathbf{X}_s)/|\mathbf{X}_r \times \mathbf{X}_s|$ is the unit vector normal to the surface $\mathbf{X}$, and the integration by parts is used to obtain the last equality. According to the principle of virtual work, the force density $\mathbf{F}$ is given by

$$\mathbf{F} = -\frac{\partial E}{\partial \mathbf{X}} = \gamma \left((\mathbf{X}_s \times \mathbf{n})_r + (\mathbf{n} \times \mathbf{X}_r)_s \right) = \gamma (\mathbf{X}_s \times \mathbf{n}_r + \mathbf{n}_s \times \mathbf{X}_r). \tag{31}$$

When the Weingarten map [31] is expressed as a matrix form with its element L_i^j for $i, j = 1, 2$ using the basis $\{\mathbf{X}_r, \mathbf{X}_s\}$, it is well known that $\mathbf{n}_r = -L_1^1 \mathbf{X}_r - L_1^2 \mathbf{X}_s$ and $\mathbf{n}_s = -L_2^1 \mathbf{X}_r - L_2^2 \mathbf{X}_s$. Thus the force density can be further simplified as

$$
\begin{aligned}
\mathbf{F} &= \gamma \left(\mathbf{X}_s \times (-L_1^1 \mathbf{X}_r - L_1^2 \mathbf{X}_s) + (-L_2^1 \mathbf{X}_r - L_2^2 \mathbf{X}_s) \times \mathbf{X}_r \right) \\
&= \gamma \left(L_1^1 + L_2^2 \right) \mathbf{X}_r \times \mathbf{X}_s \\
&= \gamma H |\mathbf{X}_r \times \mathbf{X}_s| \mathbf{n}, \tag{32}
\end{aligned}
$$

where H is the mean curvature which is the sum of the two principle curvatures. Thus, the force acting on the fluid by the immersed boundary patch $dr \, ds$ is

$$\mathbf{F} \, dr \, ds = \gamma H \left(|\mathbf{X}_r \times \mathbf{X}_s| \, dr \, ds \right) \mathbf{n}.$$

An important consequence of this derivation is that the boundary force density $\mathbf{F}$ is normal to the boundary, which is used in Section 2.

Now we derive the discretized form of force density based on a triangulation $\{T_f\}$ of the foam surface, where f is the index of triangular facets. The corresponding discrete energy functional is written as

$$E_h[\mathbf{X}] = \sum_f E_h[T_f] = \gamma \sum_f |T_f| \tag{33}$$

where $|T_f|$ is the area of triangular facet f. Let $\{\mathbf{X}_k\}$ be a collection of vertices of these triangular facets, then the force density at $\mathbf{X}_k$ can be defined as

$$\mathbf{F}_k(\triangle A)_k = -\frac{\partial E_h[\mathbf{X}]}{\partial \mathbf{X}_k} = -\gamma \frac{\partial}{\partial \mathbf{X}_k} \sum_f |T_f|.$$

Since there are only a few of triangular facets that touch $\mathbf{X}_k$, we can further simplify the above summation as

$$\mathbf{F}_k(\triangle A)_k = -\sum_{f \in \text{facets}(k)} \frac{\partial E_h[T_f]}{\partial \mathbf{X}_k}$$

where facets(k) is the set of triangular facets that touch vertex k. Therefore, it is sufficient to show how to compute force density generated from the energy functional of one triangular facet T_f. To proceed, let us denote the three vertices of facet f as $\{\mathbf{X}_{f,k,1} = \mathbf{X}_k, \mathbf{X}_{f,k,2}, \mathbf{X}_{f,k,3}\}$. Thus, the discrete energy on the facet is

$$E_h[T_f] = \gamma |T_f| = \gamma \frac{1}{2}\left|(\mathbf{X}_{f,k,2} - \mathbf{X}_k) \times (\mathbf{X}_{f,k,3} - \mathbf{X}_k)\right|. \tag{34}$$

Let $\{\mathbf{e}_1, \mathbf{e}_2, \mathbf{e}_3\}$ be the standard basis for $\mathbb{R}^3$, then the i-component of the gradient of the energy $E[T_f]$ with respect to $\mathbf{X}_k$ can be computed as follows:

$$\begin{aligned} \frac{\partial E_h[T_f]}{\partial \mathbf{X}_k} \cdot \mathbf{e}_i &= \frac{\gamma}{2} \lim_{\epsilon \to 0} \frac{|(\mathbf{X}_{f,k,2} - (\mathbf{X}_k + \epsilon \mathbf{e}_i)) \times (\mathbf{X}_{f,k,3} - (\mathbf{X}_k + \epsilon \mathbf{e}_i))| - |(\mathbf{X}_{f,k,2} - \mathbf{X}_k) \times (\mathbf{X}_{f,k,3} - \mathbf{X}_k)|}{\epsilon} \\ &= -\frac{\gamma}{2}\big((\mathbf{X}_{f,k,2} - \mathbf{X}_{f,k,3}) \times \mathbf{e}_i\big) \cdot \mathbf{n}_f \\ &= -\frac{\gamma}{2}\big((\mathbf{X}_{f,k,3} - \mathbf{X}_{f,k,2}) \times \mathbf{n}_f\big) \cdot \mathbf{e}_i, \end{aligned} \tag{35}$$

where $\mathbf{n}_f = (\mathbf{X}_{f,k,2} - \mathbf{X}_k) \times (\mathbf{X}_{f,k,3} - \mathbf{X}_k)/|(\mathbf{X}_{f,k,2} - \mathbf{X}_k) \times (\mathbf{X}_{f,k,3} - \mathbf{X}_k)|$ is the unit normal to the triangle T_f. Thus, the force acting on $\mathbf{X}_k$ generated by the discrete energy over the facet T_f can be written as

$$-\frac{\partial E_h[T_f]}{\partial \mathbf{X}_k} = \frac{\gamma}{2}(\mathbf{X}_{f,k,3} - \mathbf{X}_{f,k,2}) \times \mathbf{n}_f. \tag{36}$$

Therefore, the total force acting on $\mathbf{X}_k$ is

$$\mathbf{F}_k(\triangle A)_k = -\sum_{f \in \text{facets}(k)} \frac{\partial E_h[T_f]}{\partial \mathbf{X}_k} = \sum_{f \in \text{facets}(k)} \frac{\gamma}{2}(\mathbf{X}_{f,k,3} - \mathbf{X}_{f,k,2}) \times \mathbf{n}_f. \tag{37}$$

Note that the order of the vertices in a facet does not matter. If we interchange the subscripts 2 and 3 in the above equations, $(\mathbf{X}_{f,k,3} - \mathbf{X}_{f,k,2})$ and $\mathbf{n}_f$ both change sign, so each term in Eq. (37) remains the same as before. This equation is used in Eq. (17) in Section 3 for the force generator.

Appendix B. Discretized 3D von Neumann relation

In this appendix, we derive a discretized version of the 3D generalization of the von Neumann relation [4] for the rate of change of volume of a bubble within a dry foam. Our derivation follows an outline for how the discretization should be done as described in [32]. We give the details to point out the relationship to our scheme, and to highlight the various approximations that are made along the way. The errors in these approximations should approach zero as the resolution of the computation is refined.

For simplicity, we begin by considering an isolated bubble, i.e., a soap film in the form of a closed surface that partitions $\mathbb{R}^3$ into an interior region and an exterior region. Let $S(t)$ be the surface occupied by the soap film, and let $V(t)$ be the enclosed volume. Then,

$$\frac{dV}{dt} = M\gamma \iint\limits_{S(t)} H \, dS, \tag{38}$$

where M is the permeability of the soap film to the surrounding gas, γ is the surface tension of the soap film, H is the sum of the principal curvatures of the surface $S(t)$, and dS is the area element on $S(t)$. The sign convention for H is that inward curvature is considered negative. Thus $H = -2/R$ for a sphere of radius R.

We remark that Eq. (38) holds a quite generally, even in the presence of a background (incompressible) flow which may deform the bubble in some complicated way, so that H is not all uniform. Such a background flow makes no direct contribution to $\frac{dV}{dt}$, since $\nabla \cdot \mathbf{u} = 0$ implies that

$$\iint\limits_{S(t)} \mathbf{u} \cdot \mathbf{n} \, dS = 0. \tag{39}$$

In the present work, the surface $S(t)$ is faceted with triangular facets. Let the vertices of this triangulated surface be denoted $\mathbf{X}_k$. Then it is straightforward to show that

$$\frac{dV}{dt} = \sum_k \sum_{f \in \text{facets}(k)} \frac{1}{3} |T_f| \mathbf{n}_f \cdot \frac{d\mathbf{X}_k}{dt}, \tag{40}$$

where facets(k) is the set of triangular facets that touch vertex k, $|T_f|$ is the area of facet f, and $\mathbf{n}_f$ is the unit normal to facet f pointing toward the outside of the surface $S(t)$. Our formula for $d\mathbf{X}_k/dt$ as given in Eq. (19) is

$$\frac{d\mathbf{X}_k}{dt} = \mathbf{U}_k + M \frac{\mathbf{F}_k(\Delta A)_k}{\sum_{f \in \text{facets}(k)} \frac{1}{3} |T_f|} \tag{41}$$

where

$$\mathbf{F}_k(\Delta A)_k = -\gamma \frac{\partial}{\partial \mathbf{X}_k} \sum_f |T_f|, \tag{42}$$

and $\mathbf{U}_k$ is the interpolated fluid velocity evaluated at $\mathbf{X}_k$. As before, the expression $\sum_f |T_f|$ is the total area of the triangulated surface $S(t)$, so $\gamma \sum_f |T_f|$ is the potential energy of this surface. In our scheme, $\mathbf{F}_k$ is minus the gradient of this potential energy with respect to $\mathbf{X}_k$.

We now substitute (41) and (42) into (40), but we make the approximation of dropping the term

$$\sum_k \sum_{f \in \text{facets}(k)} \frac{1}{3} |T_f| \mathbf{n}_f \cdot \mathbf{U}_k, \tag{43}$$

which is a discretization of $\iint_{S(t)} \mathbf{u} \cdot \mathbf{n} \, dS$ (Eq. (39)), and should therefore converge to zero as the resolution of our computation is refined. With this approximation, Eq. (40) becomes

$$\frac{dV}{dt} = -M\gamma \sum_k \mathbf{N}_k \cdot \frac{\partial}{\partial \mathbf{X}_k} \sum_f |T_f|, \tag{44}$$

where

$$\mathbf{N}_k = \frac{\sum_{f \in \text{facets}(k)} \frac{1}{3} |T_f| \mathbf{n}_f}{\sum_{f \in \text{facets}(k)} \frac{1}{3} |T_f|} \tag{45}$$

is the *area-weighted normal* to the surface at the vertex k. Note that $\mathbf{N}_k$ is not, in general, a unit vector. If the faceted surface is a triangulation of a smooth surface, however, then $\mathbf{N}_k$ is approximately a unit vector and moreover approximately equal to the surface normal evaluated at the vertex $\mathbf{X}_k$. The approximation improves as the triangulation is refined.

In Appendix A, it is shown in Eq. (37) that

$$-\frac{\partial}{\partial \mathbf{X}_k} \sum_f |T_f| = \frac{1}{2} \sum_{f \in \text{facets}(k)} (\mathbf{X}_{f,k,3} - \mathbf{X}_{f,k,2}) \times \mathbf{n}_f. \tag{46}$$

Here we are using the same notation as described in Appendix A. We can reduce the right-hand side of (46) to an edge based expression by noting that

$$\mathbf{X}_{f,k,3} - \mathbf{X}_{f,k,2} = (\mathbf{X}_{f,k,3} - \mathbf{X}_{f,k,1}) - (\mathbf{X}_{f,k,2} - \mathbf{X}_{f,k,1}) = (\mathbf{X}_{f,k,3} - \mathbf{X}_k) - (\mathbf{X}_{f,k,2} - \mathbf{X}_k). \tag{47}$$

Let an index e be assigned to each edge of the faceted surface. An edge can be traversed in either of two directions. If edge e connects vertices k and l, we say that the edge vector is

$$\mathbf{Z}_e = \mathbf{X}_l - \mathbf{X}_k, \tag{48}$$

when the edge is traversed from k to l. Let $f_1(e)$ and $f_2(e)$ be the two facets that meet at edge e, and let the order of the pair $(f_1(e), f_2(e))$ depend on the direction in which the edge is traversed so that, on the outside of the surface, $f_1(e)$ is the facet to the right of the edge vector $\mathbf{Z}_e$ and $f_2(e)$ is the facet to the left. It follows that the expression

$$\mathbf{Z}_e \times (\mathbf{n}_{f_2(e)} - \mathbf{n}_{f_1(e)}) \tag{49}$$

is *independent* of the direction of traversal of the edge, since a change in direction changes the sign of $\mathbf{Z}_e$ and also interchanges $f_1(e)$ and $f_2(e)$.

In the expression (49), note that $\mathbf{Z}_e$ is orthogonal to $\mathbf{n}_{f_1(e)}$ and $\mathbf{n}_{f_2(e)}$; hence it is orthogonal to $\mathbf{n}_{f_2(e)} - \mathbf{n}_{f_1(e)}$. Let θ_e be the angle between the unit vectors $\mathbf{n}_{f_1(e)}$ and $\mathbf{n}_{f_2(e)}$, with $\theta_e > 0$ if edge e is convex when viewed from outside the surface. Then

$$\mathbf{Z}_e \times (\mathbf{n}_{f_2(e)} - \mathbf{n}_{f_1(e)}) = |\mathbf{Z}_e| 2 \sin\left(\frac{\theta_e}{2}\right) \boldsymbol{\eta}_e, \tag{50}$$

where

$$\boldsymbol{\eta}_e = \frac{\mathbf{n}_{f_1(e)} + \mathbf{n}_{f_2(e)}}{|\mathbf{n}_{f_1(e)} + \mathbf{n}_{f_2(e)}|} \tag{51}$$

can be thought of as the outward-pointing unit normal to the surface along edge e.

Making use of the above notation and results, we apply summation by parts to the right-hand side of (46), after making use of (47), to obtain

$$-\frac{\partial}{\partial \mathbf{X}_k} \sum_f |T_f| = -\frac{1}{2} \sum_{e \in \text{edges}(k)} \mathbf{Z}_e \times (\mathbf{n}_{f_2(e)} - \mathbf{n}_{f_1(e)})$$

$$= -\frac{1}{2} \sum_{e \in \text{edges}(k)} |\mathbf{Z}_e| 2 \sin\left(\frac{\theta_e}{2}\right) \boldsymbol{\eta}_e, \tag{52}$$

where edges(k) is the set of edges that touch vertex k. Substituting this result into (44) gives

$$\frac{dV}{dt} = -M\gamma \sum_k \mathbf{N}_k \cdot \frac{1}{2} \sum_{e \in \text{edges}(k)} |\mathbf{Z}_e| 2 \sin\left(\frac{\theta_e}{2}\right) \boldsymbol{\eta}_e. \tag{53}$$

At this point, we make the approximation that $\mathbf{N}_k \cdot \boldsymbol{\eta}_e \approx 1$ for $e \in \text{edges}(k)$, and also the approximation that $2 \sin(\frac{\theta_e}{2}) \approx \theta_e$. Both of these approximations improve along with the resolution of the computation, provided that the triangulated surface approaches a smooth surface as the triangulation is refined. With these approximations, Eq. (53) becomes

$$\frac{dV}{dt} = -\frac{M\gamma}{2} \sum_k \sum_{e \in \text{edges}(k)} |\mathbf{Z}_e| \theta_e = -M\gamma \sum_e |\mathbf{Z}_e| \theta_e, \tag{54}$$

where $\sum_e$ denotes the sum over all edges of the faceted surface. Note that, while each edge appears twice in the expression $\sum_k \sum_{e \in \text{edges}(k)}$, each edge appears only once in $\sum_e$. We emphasize that θ_e, the angle between the normals to adjacent facets at edge e, is a signed quantity; it is positive if the faceted surface is convex towards the outside at edge e. Eq. (54) is a well-known discretization of Eq. (38), see for example [32].

In the above derivation, we have considered an isolated bubble. For a bubble in a foam, there are special junction edges, at which three (or possibly more) surfaces meet. In our scheme, there is no permeability at vertices along junction edges. This leads to the following modification of Eq. (54).

$$\frac{dV}{dt} = -M\gamma \sum_{e \in E_0} |\mathbf{Z}_e| \theta_e - \frac{M\gamma}{2} \sum_{e \in E_1} |\mathbf{Z}_e| \theta_e, \tag{55}$$

where E_i is the set of edges which have exactly i of their two vertices on a junction edge, which is defined as an edge on which three or more facets meet. Thus E_2 is the set of junction edges; these edges do not appear in (55) at all. E_1 is the set of non-junction edges which share a vertex with a junction edge; these edges appear at half strength in (55). Finally E_0 is the set of non-junction edges which do not touch a junction edge; these appear in Eq. (55) at full strength. We use (55) as the discretized 3D von Neumann relation for comparison with our computational results.

References

[1] D. Weaire, S. Hutzler, The Physics of Foams, Oxford University Press, 1999.
[2] J. von Neumann, in: C. Herring (Ed.), Metal Interfaces, American Society for Metals, Cleveland, 1951, pp. 108–110.
[3] W.W. Mullins, in: W.D. Robertson, N.A. Gjostein (Eds.), Metal Surfaces: Structure, Energetics, and Kinetics, American Society for Metals, Metals Park, Ohio, 1963, pp. 17–66.
[4] R.D. MacPherson, D.J. Srolovitz, The von Neumann relation generalized to coarsening of three-dimensional microstructures, Nature 446 (26) (2007) 1053–1055.
[5] S. Hilgenfeldt, A.M. Kraynik, S.A. Koehler, H.A. Stone, An accurate von Neumann's law for three-dimensional foams, Phys. Rev. Lett. 86 (12) (2001) 2685–2688.

[6] D. Weaire, J.P. Kermode, Computer simulation of a two-dimensional soap froth II. Analysis of results, Philos. Mag. B 50 (1984) 379–395.
[7] J.P. Kermode, D. Weaire, 2D-froth: a program for the investigation of 2-dimensional froths, Comput. Phys. Commun. 60 (1990) 75–109.
[8] T. Herdtle, H. Aref, Numerical experiments on two-dimensional foam, J. Fluid Mech. 241 (1992) 233–260.
[9] X. Li, H. Zhou, C. Pozrikidis, A numerical study of the shearing motion of emulsions and foams, J. Fluid Mech. 286 (1995) 379–404.
[10] I.B. Bazhlekov, P.D. Anderson, H.E.H. Meijer, Nonsingular boundary integral method for deformable drops in viscous flows, Phys. Fluids 16 (4) (2004).
[11] H.J. Frost, C.V. Thompson, Computer simulation of grain growth, Curr. Opin. Solid State Mater. Sci. 1 (1996) 361–368.
[12] A.M. Kraynik, D.A. Reinelt, Foam microrheology: from honeycombs to random foams, in: Proceedings of the PPS-15, 1999.
[13] Y. Kim, M.-C. Lai, C.S. Peskin, Numerical simulations of two-dimensional foam by the immersed boundary method, J. Comput. Phys. 229 (2010) 5194–5207.
[14] Y. Kim, C.S. Peskin, 2-D parachute simulation by the Immersed Boundary Method, SIAM J. Sci. Comput. 28 (6) (2006).
[15] Y. Kim, Y. Seol, M.-C. Lai, C.S. Peskin, The immersed boundary method for two-dimensional foam with topological changes, Commun. Comput. Phys. 12 (2) (2012).
[16] C.S. Peskin, B.F. Printz, Improved volume conservation in the computation of flows with immersed elastic boundaries, J. Comput. Phys. 105 (1993) 33–46.
[17] M.-C. Lai, Z. Li, A remark on jump conditions for three-dimensional Navier–Stokes equations involving an immersed moving membrane, Appl. Math. Lett. 14 (2001) 149–154.
[18] C.S. Peskin, The immersed boundary method, Acta Numer. 11 (2002) 479–517.
[19] C.S. Peskin, D.M. McQueen, Fluid dynamics of the heart and its valves, in: Case Studies in Mathematical Modeling: Ecology, Physiology, and Cell Biology, Prentice Hall, Englewood Cliffs, NJ, 1996, pp. 309–337.
[20] D. Goldstein, R. Handler, L. Sirovich, Modeling a no-slip flow with an external force field, J. Comput. Phys. 105 (1993) 354.
[21] E.M. Saiki, S. Biringen, Numerical simulation of a cylinder in uniform flow: application of a virtual boundary method, J. Comput. Phys. 123 (2) (1996) 450–465.
[22] K. Chen, K. Feng, Y. Kim, M.-C. Lai, A note on pressure accuracy in immersed boundary method for Stokes flow, J. Comput. Phys. 230 (2011) 4377–4383.
[23] Y. Kim, C.S. Peskin, Penalty immersed boundary method with an elastic boundary with mass, Phys. Fluids 19 (5) (May 2007).
[24] B.E. Griffith, C.S. Peskin, On the order of accuracy of the immersed boundary method: higher order convergence rates for sufficiently smooth problems, J. Comput. Phys. 208 (2005) 75–105.
[25] C.H. Rycroft, Voro++: a three-dimensional Voronoi cell library in C++, Chaos 19 (2009) 041111.
[26] J.A. Glazier, Grain growth in three dimensions depends on grain topology, Phys. Rev. Lett. 70 (14) (1993) 2170–2173.
[27] Clément Sire, Growth laws for 3D soap bubbles, Phys. Rev. Lett. 72 (3) (1994) 420–423.
[28] C. Monnereau, M. Vignes-Adler, Dynamics of 3D real foam coarsening, Phys. Rev. Lett. 80 (23) (1998) 5231–5288.
[29] G.L. Thomas, R.M.C. de Almeida, Coarsening of three-dimensional grains in crystals, or bubbles in dry foams, tends towards a universal, statistically scale-invariant regime, Phys. Rev. E 74 (2006) 021407.
[30] J. Lambert, R. Mokso, I. Cantat, P. Cloetens, J.A. Glazier, F. Graner, R. Delannay, Coarsening foams robustly reach a self-similar growth regime, Phys. Rev. Lett. 104 (24) (2010).
[31] M. DoCarmo, Differential Geometry of Curves and Surfaces, International Edition, Pearson, 2009.
[32] J.M. Sullivan, Curvatures of smooth and discrete surfaces, in: Discrete Differential Geometry, in: Oberwolfach Semin., vol. 38, Birkhäuser, Basel, 2008, pp. 175–188.